12

EDGEWOOD
RESEARCH,
DEVELOPMENT &
ENGINEERING
CENTER

ERDEC-TR-127

CHAMBER OPTICS FOR TESTING PASSIVE REMOTE SENSING VAPOR DETECTORS

Dennis F. Flanigan

RESEARCH AND TECHNOLOGY DIRECTORATE

November 1993

U.S. ARMY
CHEMICAL
AND BIOLOGICAL
DEFENSE AGENCY

Aberdeen Proving Ground, Maryland 21010-5423

Disclaimer

The findings in this report are not to be construed as an official Department of the Army position unless so designated by other authorizing documents.

REPORT DOCUMENTATION PAGE

Form Approved
OMB No. 0704-0188

1. AGENCY USE ONLY (Leave blank)	2. REPORT DATE	3. REPORT TYPE AND DATES COVERED
	1993 November	Final, 93 Jan - 93 Jun

4. TITLE AND SUBTITLE
Chamber Optics for Testing Passive Remote Sensing Vapor Detectors

5. FUNDING NUMBERS
PR-10463806D601

6. AUTHOR(S)
Flanigan, Dennis F.

7. PERFORMING ORGANIZATION NAME(S) AND ADDRESS(ES)
DIR, ERDEC, ATTN: SCBRD-RTM, APG, MD 21010-5423

8. PERFORMING ORGANIZATION REPORT NUMBER
ERDEC-TR-127

9. SPONSORING/MONITORING AGENCY NAME(S) AND ADDRESS(ES)

10. SPONSORING/MONITORING AGENCY REPORT NUMBER

11. SUPPLEMENTARY NOTES

12a. DISTRIBUTION/AVAILABILITY STATEMENT
Approved for public release; distribution is unlimited.

12b. DISTRIBUTION CODE

13. ABSTRACT (Maximum 200 words)

There is a need to test the response of multiple remote sensing FTS to known concentrations of vapors with a carefully controlled temperature difference, ΔT, between a background source, Tbg, and the gas, Tg. We have analyzed the various factors inherent in delivering a beam of specified radiance to the sensor including: the geometrical factors needed to assure that the background source fills the field-of-view, methods of multisensor viewing and the effects of the transmittance of the additional optical elements. Several optical configurations will deliver a suitable beam. The telescopically based system delivers a spatially similar beam to what the sensor would see in the field. The 2 lens system delivers an image at the entrance aperture that is functionally equivalent to a collimated beam at least for single detector spectroradiometers. The radiance analysis showed that the position of the optical elements is important. These results suggest that there is very little penalty to a one window cell, which might be substantially easier to design and build than a windowless cell. This effort has been completely analytical; experimental verification is planned for the coming year.

14. SUBJECT TERMS		15. NUMBER OF PAGES
Infrared	Spectroradiometry	58
Etendue	Radiance	16. PRICE CODE
Geometrical optics	Telescope	

17. SECURITY CLASSIFICATION OF REPORT	18. SECURITY CLASSIFICATION OF THIS PAGE	19. SECURITY CLASSIFICATION OF ABSTRACT	20. LIMITATION OF ABSTRACT
UNCLASSIFIED	UNCLASSIFIED	UNCLASSIFIED	UL

Blank

PREFACE

The work described in this report was authorized under Project No. 10463806D601, Chemical Detection and Warning. The work was started in January 1993 and completed in June 1993.

The use of trade names or manufacturers' names in this report does not constitute an official endorsement of any commercial products. This report may not be cited for purposes of advertisement.

This report has been approved for release to the public. Registered users should request additional copies from the Defense Technical Information Center; unregistered users should direct such requests to the National Technical Information Service.

Blank

CONTENTS

LIST OF FIGURES

LIST OF TABLES

Chamber Optics for Testing Passive Remote Sensing Vapor Detectors

1.0 The "Risk Reduction" Experiment

There is a requirement [1] to test the response of passive infrared (IR) remote sensing vapor detectors, in particular the XM21, to known concentrations of vapors with a carefully controlled temperature difference, ΔT, between a background source at temperature, T_{bg}, and the gas at T_g. There are additional constraints on this test including the requirement that 2 or more sensors must view the same gas volume simultaneously to correlate detector response. Our immediate purpose is to analyze various optical factors inherent in designing a optical system to assure that the experimental design accurately delivers a radiance characteristic of a specified ΔT for the XM21 experiments. Our longer range goals are to establish the basics of the optical systems useful for future experiments with passive IR sensors.

Figure 1 shows the XM21 portion of the proposed optical design of the Risk Reduction Plan (RRP) experiment.[2] Other parts of the design cover analytical transmissometers. Gladden and Marshall propose a 2 lens system to image the background source onto the entrance aperture of the XM21. Beam splitters would be used to direct the radiation to multiple XM21's. This design, re drawn from Figure 4 of the DPG Methodology Test Report, needs further analysis in the following areas: 1) The optical train, 2) the sources of radiation, 3) radiation losses and gains introduced by the beamsplitters

All distances are given in centimeters (cm) unless otherwise stated. Temperatures are in degrees Kelvin or centigrade. Angles are in degrees, radians and milliradians (mr). Solid angles are in steradians (sr).

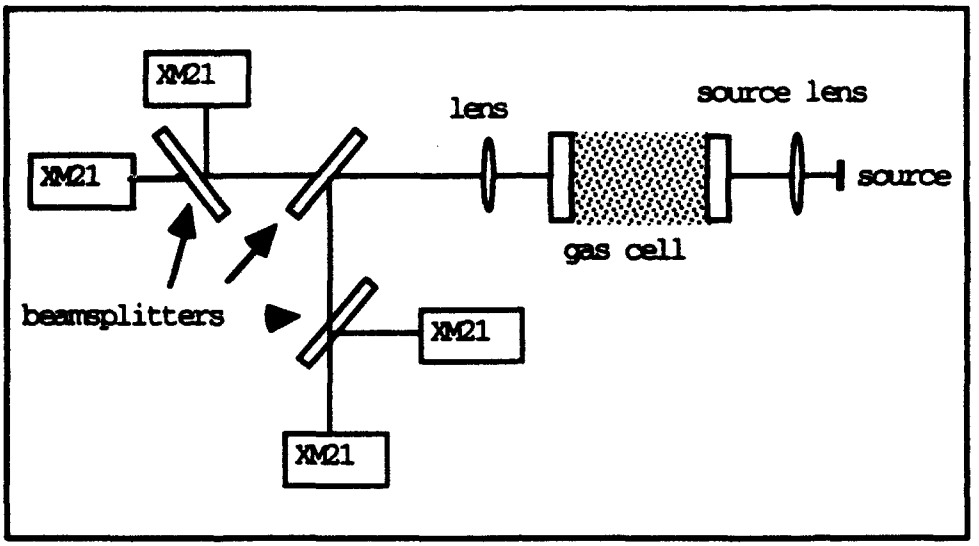

Figure 1. The XM21 portion of the optical design of the RRP chamber.

2.0 Power

The power, P_d, within in the FOV, in watts (w), collected by a passive IR remote sensing detector is[3]

$$P_d = \Im_s \tau_s L \qquad (1)$$

where $\Im_S$ is the optical throughput or étendue (cm^2 sr), τ_S is the total transmittance (unitless) of the sensor optics, and L is the radiance ($w/(cm^2 sr)$) incident on the entrance aperture, provided that the wave front from the source fills the entrance aperture of the sensor (almost never a problem with natural sources) and the source fills the FOV of the sensor. τ_S, the transmittance of the sensor optics, is quantity between 0 and 1, normally less than 0.25, that describes the fraction of energy transmitted by the sensor optics; τ_S is not dependent on sensor geometry. While of importance to system sensitivity the design of the experiment does not effect this parameter in a way that improves or degrades sensor performance. The étendue, $\Im_S$, is a measure of optical systems ability to collect radiation based on geometrical optics. It is generally accepted that étendue and radiance are the most useful concepts in analyzing the

radiometric performance of the sensor. The étendue limits the amount of power that the sensor can focus on to the detector from a beam of specified radiance. One of the goals of this effort is to ensure that the radiation field of the source fills both the entrance aperture and field-of-view (FOV) of the XM21, thus insuring maximum étendue; beyond that there is nothing to be gained. In this analysis, we will separate the geometrical optical effects from the transmission/emission effects. The optical train will be modeled and programmed in a spreadsheet; various configurations will analyzed and the minimum (limiting) étendue will be selected. This, of course, should be the sensor étendue. If it isn't, the external optics should be redesigned. Radiance, transmission and emission effects will be independently analyzed.

The radiance, L, is the effective total of the radiance's from the source and intervening elements. ΔL is defined as the radiance difference between the background, at temperature, T_{bg}, and the radiance of the target gas at temperature, T_g.

$$\Delta L = L_{bg} - L_g \tag{2}$$

or delta power, ΔP

$$\Delta P = \Im_s \tau_s \Delta L \tag{3}$$

ΔL will be diminished by the optics of this experiment. During an early phase of this effort there was some speculation on making up reflectance losses using by increasing the size and focusing power of the optics; this is impossible. The fundamental theorem of radiometry[4] states that: "*there is no optical system that can increase the effective radiance of the source*". Losses caused by intervening optics can only be offset by increasing the actual radiance of the source, e.g., in the case of thermal sources, by increasing source temperature. Our objective is to analyze various optical configurations and determine the required increase in T_{bg}. The approach will be to compute ΔP in the absence of optically induced losses and then compute T_{bg} needed to sustain ΔP in the presence of the losses.

3.0 Étendue

3.1 Definition of Étendue

The étendue[5,6] or throughput, $\Im$, can be defined in 3 ways (See figure 2.)

$$\Im = \iint \frac{\cos\theta_1 dA_1 \cos\theta_2 dA_2}{s^2} \qquad (4)$$

$$\Im = \iint \cos\theta_1 dA_1 d\Omega_1 \qquad (5)$$

$$\Im = \iint \cos\theta_2 dA_2 d\Omega_2 \qquad (6)$$

where θ_1 and θ_2 refer to angle of the normal to the beam areas, dA_1 and dA_2, and the optical axis; Ω_1 and Ω_2 are solid angles and s is the distance between elements. Each element has a projected area. The product of one of these solid angles and the area of the associated element is the étendue. If the distance separating the elemental areas is 10 or more times greater the diameter of the elements, then the integral expression can be replaced by

$$\Im = A_1\Omega_2 = \frac{A_1 A_2}{f^2} \qquad (7)$$

with only a few percent error, where f is the distance between elements, frequently the focal length. If solid angles are large, e.g. the final lens which focuses the radiation on the detector is "faster" than f/3 or f/4, the more rigorous solid angle expression, that results from integration is

$$\Im = A\ \pi \sin^2\phi \qquad (8)$$

where ϕ is the angle from the center line to the edge of the element.

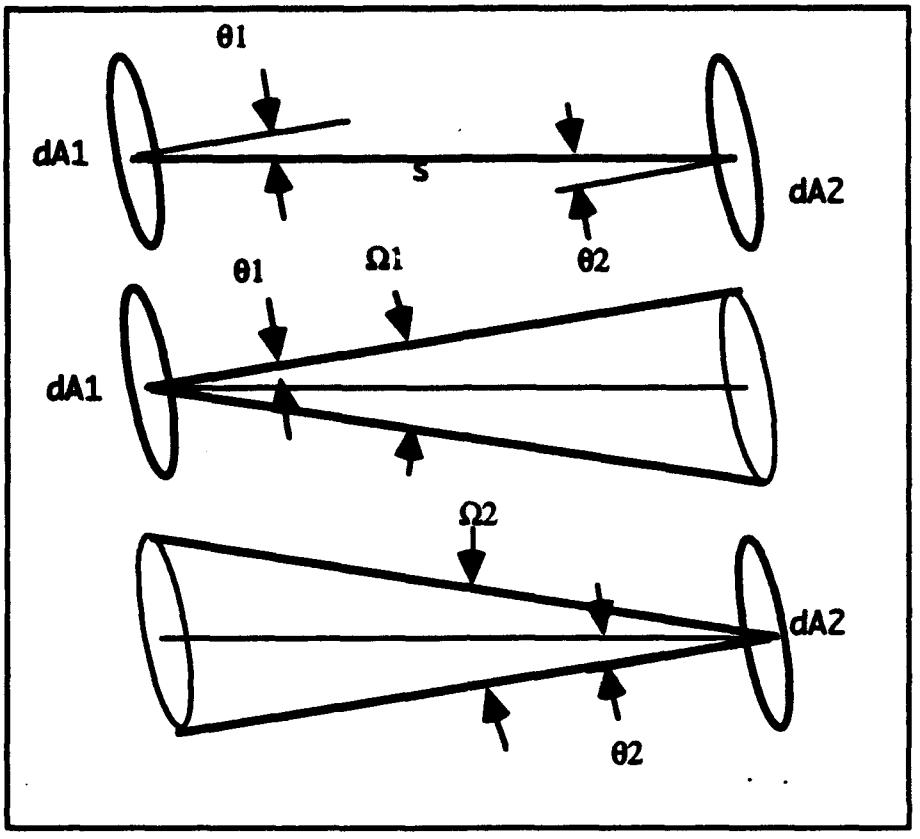

Figure 2. The different ways of defining étendue

The general rule for which equation to use, 7 or 8, is based on relative separation to element size. If the separation is greater than 10 X element areas, then the difference in predicted étendue is small. Figure 3 shows étendues computed by the 2 methods.

What happens if the elements differ substantially in size? What element should be chosen as the area component and what should be used to define the solid angle? Figure 4 shows the étendue as a function of radius 1 for a element-element separation of 2, unit radius for element 2 and a radius varying from .1 to 1.1 for element 1. The 3 methods of computing, area-angle, angle-area and area-area, were used. It can be seen that the area-angle and angle-area do not produce identical results, but it is not clear which method is superior; the agreement between both predictions is much better than either with the area-area technique in regions of equivalent radius, but much less clear in regions of substantial size

difference. The angle-area method was used for these calculations, where the angle is known as the angle-of-projection[7].

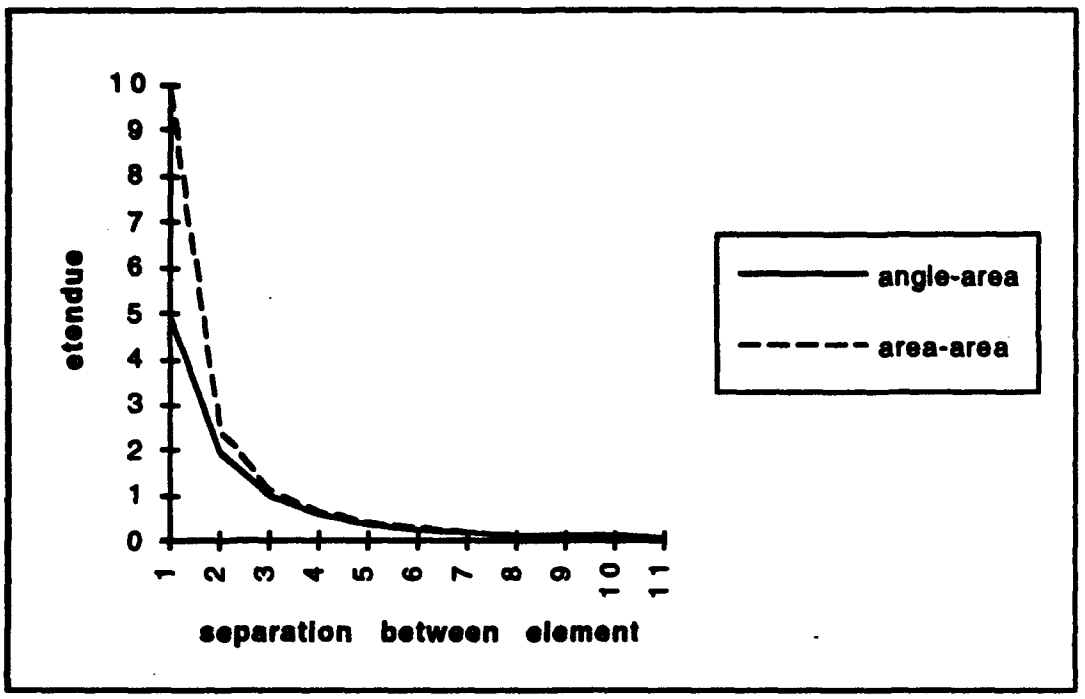

Figure 3. Predicted étendues for elements of unit radius from equations 7 & 8

3.2 Ray Tracing

In order to determine the required étendue at each section in the optical system some technique is required to compute the beam diameter at every element within the optical path. A number of methods, some ad hoc, were tried; ray tracing proved to be the most useful. Rays were iteratively traced through every element using the following paraxial equations.[8]

$$u_n' = u_n + \frac{y_n}{f_n} \tag{9}$$

$$y_{n+1} = y_n - d_n' u_n' \tag{10}$$

where u_n is the slope of the ray entering the nth optical element, y_n is the height of the ray above the optical axis, on the nth element, f_n is

the focal length of the nth element and u_n' is the slope of the ray exiting the nth element. d_n' is the distance to the n+1th element, and y_{n+1} is the height of the ray on the n+1th optical element. Sign conventions are in ref 7 in detail. The only unusual convention was the slope sign; it is positive if the ray is rotated counterclockwise to reach the axis. The specific details will be discussed under each configuration.

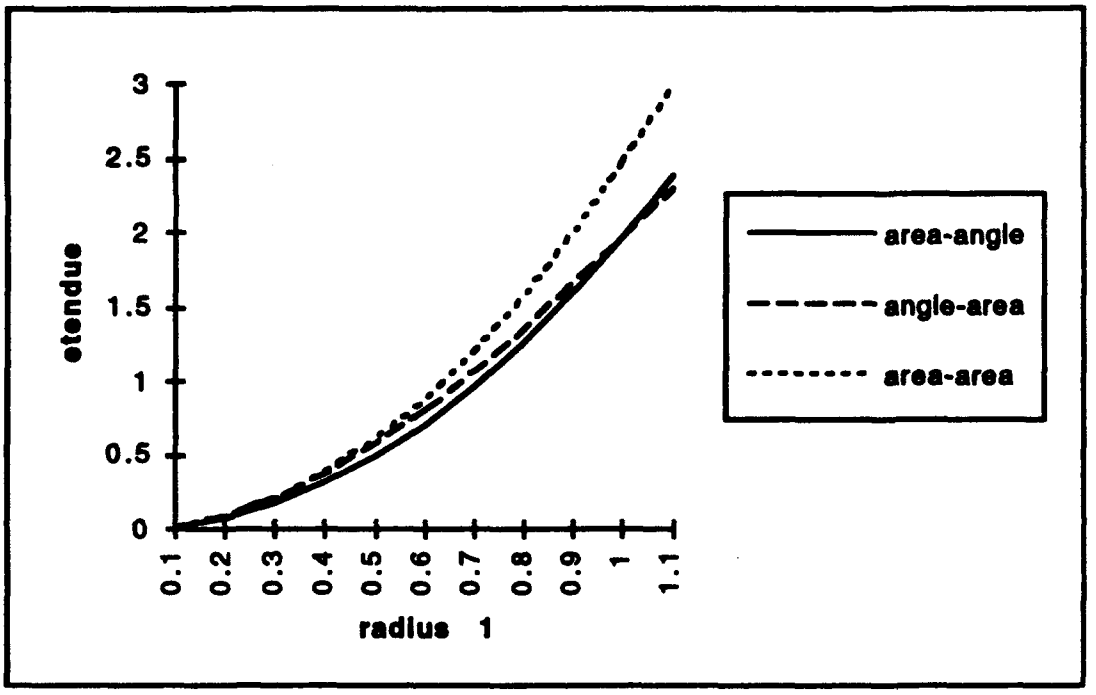

Figure 4. Étendue as a function element 1 radius. Element 2 is unit radius and the spacing is 2.

3.3 Field-of-View

The field-of-view (FOV) for visual optical systems, e.g. binoculars, is given in lateral distance at some range. For this type of system, the FOV is usually defined as the projection of a limiting stop into the object plane. FOV is more easily visualized for single element sensor, focused at infinity, as the angle formed by lines through the center of the lens to the edges of the first stop located at the focal point of the collector. See figure 5.

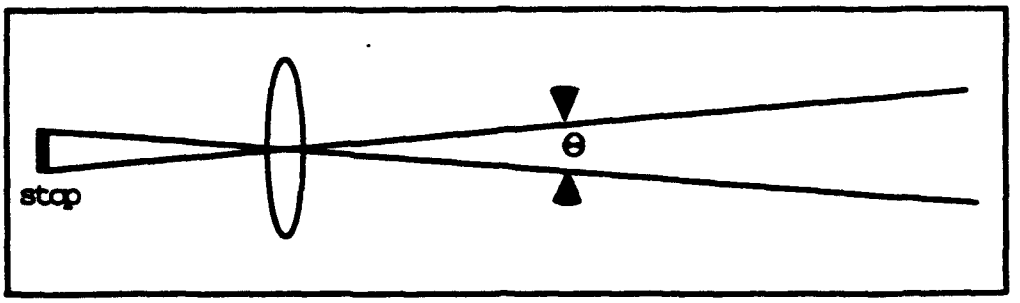

Figure 5. The boundaries of rays going through the center of the lens and the edges of the stop located at the focal point of the collector form the FOV.

For small angles, the 2 dimensional angular FOV, Θ, is

$$\Theta = \frac{D_{fl}}{f} \tag{11}$$

The solid angle FOV is approximately

$$\Omega = \frac{D_{fl}^2}{f^2} \tag{12}$$

There are further considerations that can improve our understanding of the radiation field that the single element spectral sensor is designed to accept. The sensor is focused at infinity when the field stop is located at the focal point. It will focus all rays incident at a given angle to a single point in the image plane. All rays falling within an angle equal to $1/2\Theta$ will be brought to focus within the field stop. All rays incident at a greater angle will be focused outside the FOV, *no matter where they hit the lens*. See figure 6.

The result is that the actual lateral FOV is larger, than the Θ would predict, by the diameter of the collector. This is no consequence at a distance, but can be significant at the ranges envisioned in laboratory experiments. From inspection of figure 7, the lateral FOV, D_{FOV}, at distance S is

$$D_{FOV} = D_c + \Theta S \qquad (13)$$

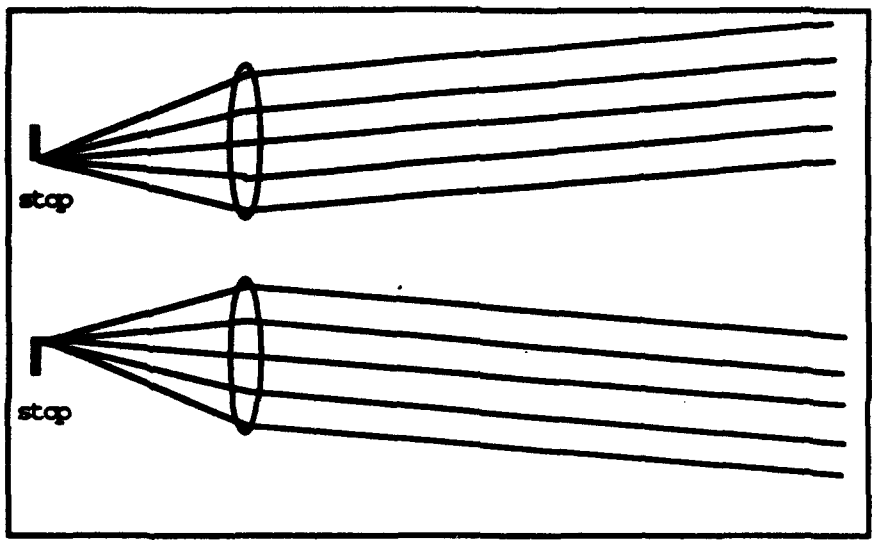

Figure 6. All rays hitting the lens at a fixed angle about the optical axis will be focused to the same point. If the angle is no greater than half the FOV the point will be within the stop.

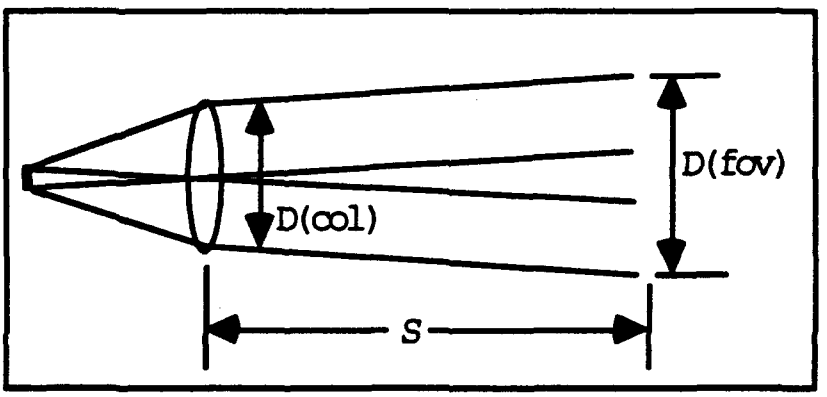

Figure 7. The angular Field-of-View (FOV) is defined by the diameter of the detector and the focal length of the collector. The lateral FOV at distance S includes the diameter of the collector lens.

Care should be taken to insure that the background source fills the sensor FOV for several reasons: 1) If the source does not fill the area surrounding the source will contribute to the signal, but only the source is well defined in temperature and emissivity. 2) The sensor may partially see the walls of the cell, which probably will not be well characterized,

and may substantially shorten the average path length and thus the average concentration-pathlength product (cl). Therefore the source must be at least as large at the lateral FOV at the experimental range; if it is smaller, than it must be expanded optically.

3.4 The XM21 Optical Design

The details of the XM21 optical system are given in the Technical Data Package (TDP)[9]; optical scematics and design goals are shown in the "XM21 Design Status Review".[10] (Only one copy of the "XM21 Design Status Review" is known to exist; it was located as a result of Webb reviewing an early draft of this report. Some of the information in that Review is reproduced in the Appendix to make it easier for future investigators to obtain essential information.) The geometry of the XM21 optics is as shown in figure 8. The optical train consists of a entrance window, a scanning mirror, an interferometer followed by a collecting lens (the exit lens in XM21 documentation), which focuses incoming radiation, falling within the solid angle of the sensor FOV, through a detector window onto a field lens[11] which refocuses the radiation onto the detector. The field lens and the detector are small, a few mm, relative to the collector, which has a diameter, D_O, of 2.65 cm (a little larger than 1 in). The FOV, Θ, is specified to be 1.5°(26 mr) both vertically and horizontally. Figure 9 shows the lateral FOV as a function of range.

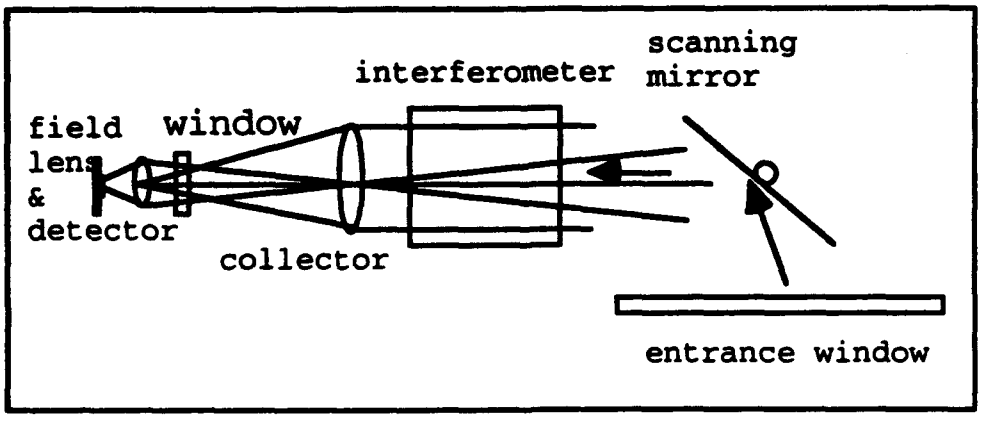

Figure 8. The internal optics of the XM21. The field lens and the detector are small and close together when compared to the collector.

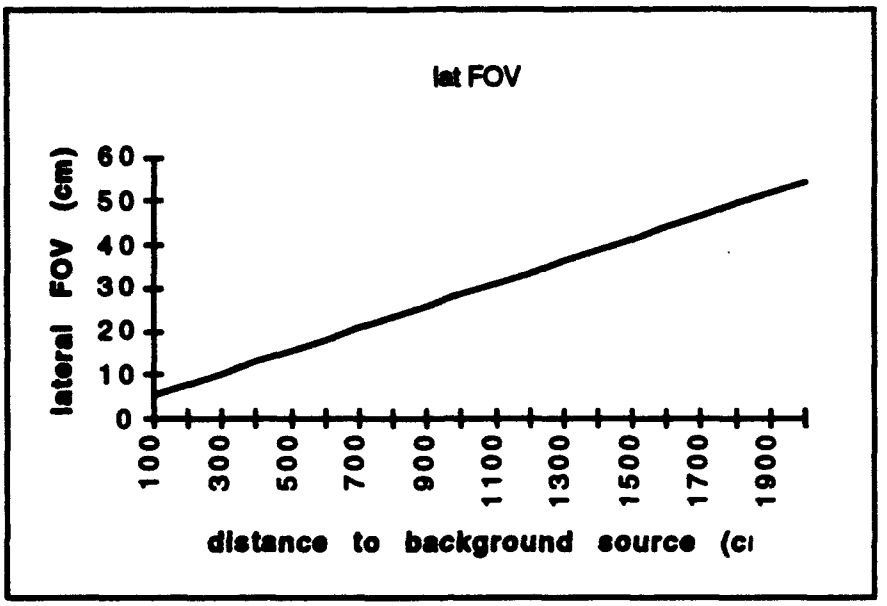

Figure 9. The lateral D_{FOV} of the XM21 from 100 to 20 meters.

The focal length for a thick lens was computed from[12]

$$\frac{1}{f} = (n-1)\left[\frac{1}{R_1} - \frac{1}{R_2} + \frac{t(n-1)}{nR_1R_2}\right] \qquad (14)$$

Drawing 5-15-10601 of the TDP specifies the collector (exit) lens as zinc selenide, radii of curvature of R_1 = 2.795" and R_2 = 8.006". Lens thickness, t, at the center is 0.160". The OSA Handbook of Optics,[13] gives the refractive index, n, of zinc selenide as 2.407 at 10 μm (1000 cm^{-1}). Using these values eq 14 predicts that focal length of the collector, f_C = 7.61 cm. Drawing 5-15-10876 shows the field lens to be in a housing with a square aperture 0.198 cm (0.078"). Θ computes to be 0.026 radians, exactly 1.5°. The object distance, S, is the focal length of the collector, 7.61 cm. The focal length of the field lens was also computed from equation 14 from data given in reference 10. The field lens is germanium (refractive index 4.003 from the OSA Handbook of Optics[14]), with radii of curvature of 4.926 cm and 6.236 cm. The lens thickness 0.1219 cm. From these values the focal length is 0.2536 cm. The field lens focuses the collector (2.65 cm)

onto the detector, whose size 0.07 cm. The image distance, S', can be calculated from the magnification requirement

$$S' = \frac{D_f}{D_c} S \qquad (15)$$

to be 0.201 cm.

The width of the beam was investigated by ray tracing with the aid of the spreadsheet, Microsoft Excel™. See table 1A. The information given in the top 4 rows, the element, its focal length, diameter and distance to the next element, are fixed as part of the design. The next 6 rows are traces of 3 rays; each pair consisting of a ray height and slope. The collector/field lens section was considered to be the controlling section. The controlling rays are defined from the top edge of the field lens to top, center and bottom of the collector. They are traced back to the detector and forward to the background source. The beam and minimum diameters, given in rows 11 and 12, are identical with the element diameters for this section. The sign of the slopes were chosen in accordance with the conventions given in ref 7 and checked with simple, easily envisioned conditions. The angle-of-projection and étendue formulas are given in rows 13 and 14. These quantities are defined in terms of the element number of the column that they fall in and the next element. Finally in row 15 the minimum étendue is selected.

Numerical values for Table 1A are shown in Table 1B. The The sensor values shown in rows 2-4 are those of the XM21 computed earlier. The next 6 rows show the 3 rays, which leave the collector at identical slopes, but laterally displaced as expected. The collector is inversely imaged on to the detector, again, as expected. The field lens/collector section has the minimum étendue. The spreadsheet was also used to make a basic plot of the rays; the distance between elements is shown as equal, not in accordance with the actual greatly differing distances, but still useful for visualization. Figure 10 shows the ray trace for the sensor.

element, n	1, detector	2, field lens	3, collector
D_n, element dia	D_1	D_2	D_3
S_n, dis next el	S_1	S_2	n/a
pY_n	$pY_2 - S_1 pU_1$	$D_2/2$	$pY_2 - S_2 pU_2$
pU_n	$-(pU_2) + \frac{pY_2}{F_2}$	$\frac{-(D_3 - D_2)}{2S_2}$	$pU_2 + \frac{pY_3}{F_3}$
mY_n	$mY_2 - S_1 mU_1$	$D_2/2$	$mY_2 - S_2 mU_2$
mU_n	$-(mU_2) + \frac{mY_2}{F_2}$	$\frac{-(-D_2)}{2S_2}$	$mU_2 + \frac{mY_3}{F_3}$
nY_n	$nY_2 - S_1 nU_1$	$D_2/2$	$nY_2 - S_2 nU_2$
nU_n	$-(nU_2) + \frac{nY_2}{F_2}$	$\frac{-(-D_3 - D_2)}{2S_2}$	$nU_2 + \frac{nY_3}{F_3}$
B_n, beam diameter	$2\max(\lvert pY_1 \rvert, \lvert mY_1 \rvert, \lvert nY_1 \rvert)$	D_2	D_3
D_n'', min diameter	$\min(B_1, D_1)$	D_2	D_3
θ_n, angle of projection	$\arctan\frac{D_1''}{2S_1}$	$\arctan\frac{D_2''}{2S_2}$	n/a
$\mathfrak{I}_n$, étendue	$\pi D_2^2 \sin^2\theta_1$	$\pi^2 \frac{D_3^2}{4} \sin^2\theta_2$	n/a
$\mathfrak{I}_{min}$, minimum étendue	$\min(\mathfrak{I}_2, \mathfrak{I}_2)$	n/a	n/a

Table 1A. Layout of a spreadsheet to compute the geometrical optical properties of the XM21

element	detector	field_lens	collector
fl	n/a	0.2536	7.61
el_dia	0.07	0.198	2.65
dis_nx_el	0.201	7.61	0
pY	-0.011848	0.099	1.325
pU	0.55148236	-0.1611038	0.0130092
mY	0.02314876	0.099	0
mU	0.37736935	0.0130092	0.0130092
nY	0.05814548	0.099	-1.325
nU	0.20325634	0.18712221	0.0130092
beam_dia	0.11629095	0.198	2.65
min_dia	0.07	0.198	2.65
theta	0.17240077	0.01300846	
etendue	0.00362453	0.00293197	
min_etendue	0.00293197		

Table 1B. Results of the spreadsheet computation of the geometrical optical properties of the XM21

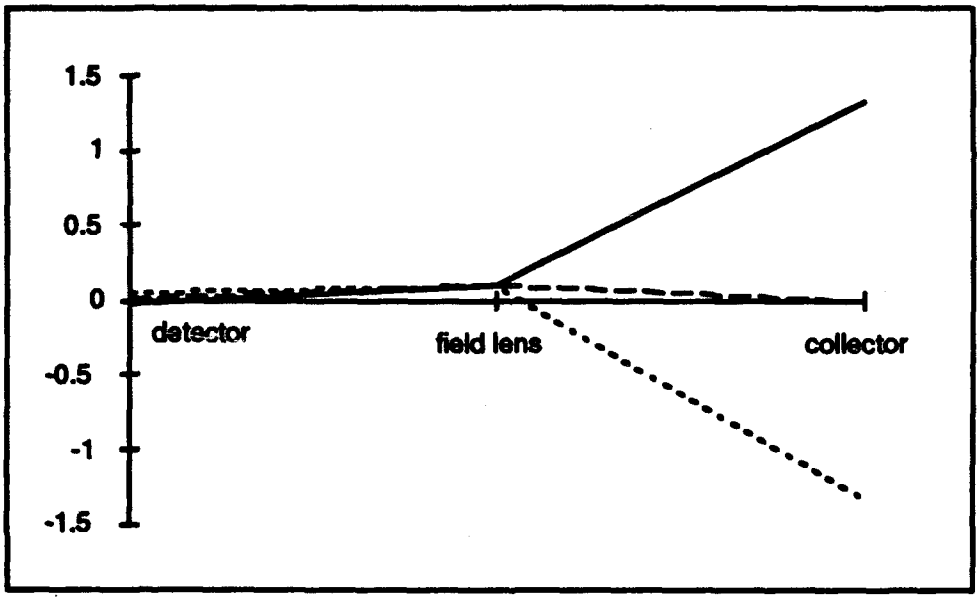

Figure 10. Ray trace of the XM21 sensor from table 1B. Distances between elements are shown as equal for convenience. Actual distances are given in the spreadsheet.

element, n	1, detector	2, field lens	3, collector	4,source
F_n, focal length	n/a	F_2	F_3	n/a
D_n, element dia	D_1	D_2	D_3	D_4
S_n, dis next el	S_1	S_2	S_3	
pY_n	$pY_2 - S_1 pU_1$	$D_2/2$	$pY_2 - S_2 pU_2$	$pY_3 - S_3 pU_3$
pU_n	$-(pU_2) + \frac{pY_2}{F_2}$	$\frac{-(D_3 - D_1)}{2S_2}$	$pU_2 + \frac{pY_2}{F_2}$	
mY_n	$mY_2 - S_1 mU_1$	$D_2/2$	$mY_2 - S_2 mU_2$	$mY_3 - S_3 mU_3$
mU_n	$-(mU_2) + \frac{mY_2}{F_2}$	$\frac{-(-D_1)}{2S_2}$	$mU_2 + \frac{mY_2}{F_2}$	
nY_n	$nY_2 - S_1 nU_1$	$D_2/2$	$nY_2 - S_2 nU_2$	$nY_3 - S_3 nU_3$
nU_n	$-(nU_2) + \frac{nY_2}{F_2}$	$\frac{-(-D_3 - D_1)}{2S_2}$	$nU_2 + \frac{nY_2}{F_2}$	
B_n, beam diameter	$2\max(\lvert pY_1\rvert, \lvert mY_1\rvert, \lvert nY_1\rvert)$	D_2	D_3	$2\max(\lvert pY_4\rvert, \lvert mY_4\rvert, \lvert nY_4\rvert)$
D_n'', min diameter	$\min(B_1, D_1)$	D_2	D_3	$\min(B_4, D_4)$
θ_n, angle of projection	$\arctan\frac{D_1''}{2S_1}$	$\arctan\frac{D_2''}{2S_2}$	$\arctan\frac{D_3''}{2S_3}$	
$\mathfrak{I}_n$, étendue	$\pi D_1''^2 \sin^2\theta_1$	$\pi^2 \frac{D_2''^2}{4} \sin^2\theta_2$	$\pi^2 \frac{D_3''^2}{4} \sin^2\theta_3$	
$\mathfrak{I}_{min}$, minimum étendue	$\min(\mathfrak{I}_1, \mathfrak{I}_2, \mathfrak{I}_3)$			

Table 2A. Layout of the spreadsheet to compute the geometrical optical properties of the sensor and an external source.

element	detector	field_lens	collector	source
fl	n/a	0.2536	7.61	n/a
el_dia	0.07	0.198	2.65	10
dis_nx_el	0.201	7.61	1000	
pY	-0.011848	0.099	1.325	-11.684198
pU	0.55148236	-0.1611038	0.0130092	
mY	0.02314876	0.099	0	-13.009198
mU	0.37736935	0.0130092	0.0130092	
nY	0.05814548	0.099	-1.325	-14.334198
nU	0.20325634	0.18712221	0.0130092	
beam_dia	0.11629095	0.198	2.65	28.6683968
min_dia	0.07	0.198	2.65	10
theta	0.17240077	0.01300846	0.001325	
etendue	0.00362453	0.00293197	0.00043318	
min_etendue	0.00043318			

Table 2B.Values for spreadsheet 2A. XM21 sensor to source located at 10 m.

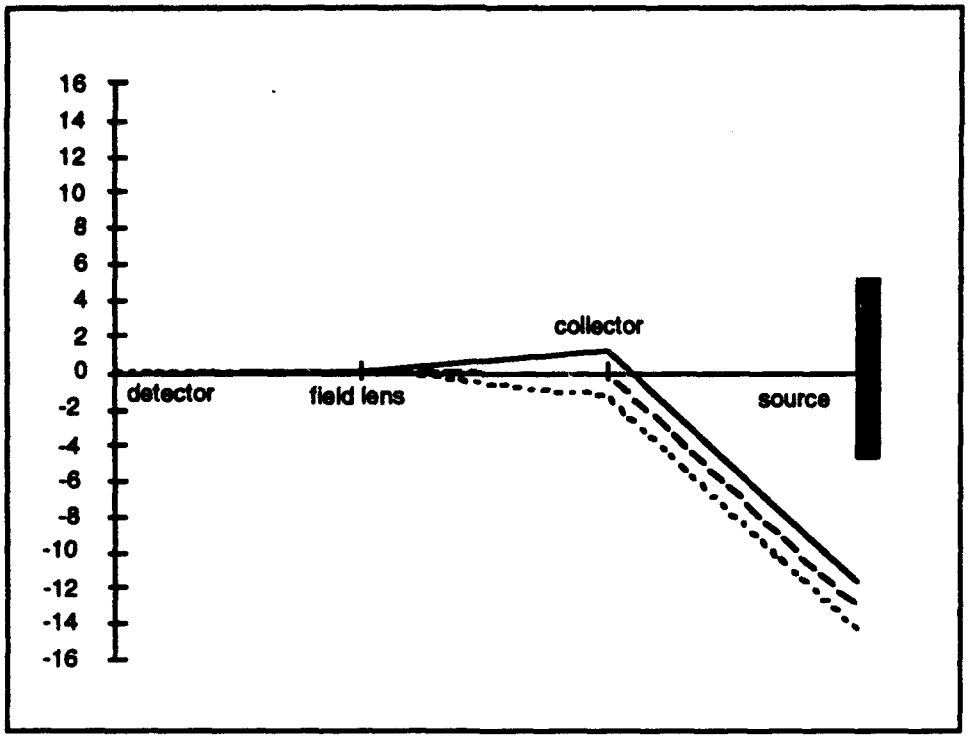

Figure 11. XM21 rays trace miss the 10 cm source.

3.5 Adding the Source

Table 2 shows the spreadsheet layout with the source included. Here the distance to the source is chosen to be 10 m. Figure 11 shows the 3 rays traced to a source located 10 m away. Note that rays from a single point on the field lens travel parallel to each other and terminate at different points on the source indicating that there will be some blur to the FOV. For this particular experiment the source is about 10 cm in diameter, considerably smaller than FOV.

3.6 Expanding the Source

The source may be expanded with a lens or mirror. If a source is placed at the focal point of a lens, the lens will collimate radiation coming from a point on the source. Using figure 12, we will show that collimating the source effectively increases the size of the source and, except for transmittance losses, the radiance is unchanged.

In figure 12 the irradiance on the source lens is:

$$E_2 = L_1 \frac{A_1}{S_1^2} = L_1 \Omega_{A_1} \tag{16}$$

The collimated beam emerging from the source lens will be diverging by the solid angle, Ω_{A1}, therefore the radiance exiting the source lens is:

$$L_2 = \frac{E_2}{\Omega_{A_1}} = \frac{L_1 \Omega_{A_1}}{\Omega_{A_1}} = L_1 \tag{17}$$

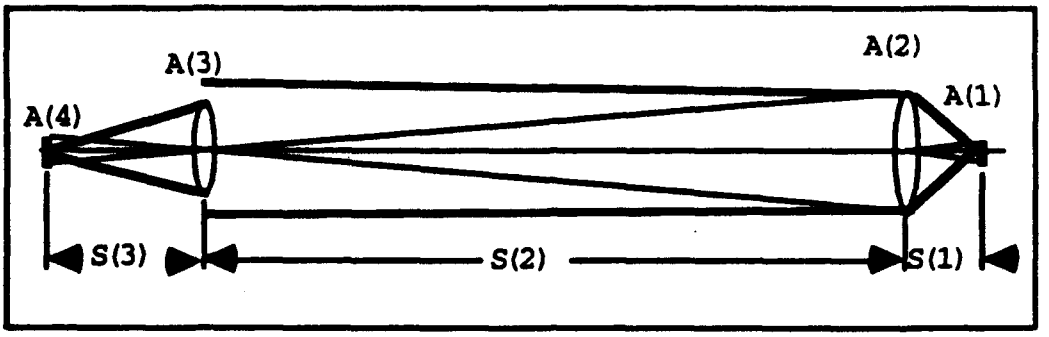

Figure 12. A source of area, A_1, with collimating lens, A_2, a collector, A_3, and detector (or field lens) A_4. Diverging and converging fields are shown in broad lines and FOV's are shown in light lines.

The irradiance over the sensor collector area, A_3, is:

$$E_3 = \frac{L_1 A_2}{S_2^2} = L_1 \Omega_{A_2} \tag{18}$$

provided that the collimated beam at least fills the collector. But the radiance emerging from the collector is the irradiance divided by the angle of divergence, which is solid angle of the source.

$$L_3 = \frac{E_3}{\Omega_{A_2}} = \frac{L_1 \Omega_{A_2}}{\Omega_{A_2}} = L_1 \tag{19}$$

Again the radiance is equal to L_1, discounting transmittance losses. In the final stage the collector lens focuses the beam into an area, A_4, of irradiance E_4.

$$E_4 = \frac{L_1 A_3}{S_3^2} = L_1 \Omega_{A_3} \tag{20}$$

element, n	1, detector	2, field lens	3, collector	4,source lens	5, source
F_n, focal length	n/a	F_2	F_3	F_4	n/a
D_n, element dia	D_1	D_2	D_3	D_4	D_5
S_n, dis next el	S_1	S_2	S_3	S_4	
pY_n	$pY_2 - S_1 pU_1$	$D_2/2$	$pY_2 - S_2 pU_2$	$pY_3 - S_3 pU_3$	$pY_4 - S_4 pU_4$
pU_n	$-(pU_2) + \frac{pY_2}{F_2}$	$\frac{-(D_3 - D_2)}{2S_2}$	$pU_2 + \frac{pY_3}{F_3}$	$pU_3 + \frac{pY_4}{F_4}$	
mY_n	$mY_2 - S_1 mU_1$	$D_2/2$	$mY_2 - S_2 mU_2$	$mY_3 - S_3 mU_3$	$mY_4 - S_4 mU_4$
mU_n	$-(mU_2) + \frac{mY_2}{F_2}$	$\frac{-(-D_2)}{2S_2}$	$mU_2 + \frac{mY_3}{F_3}$	$mU_3 + \frac{mY_4}{F_4}$	
nY_n	$nY_2 - S_1 nU_1$	$D_2/2$	$nY_2 - S_2 nU_2$	$nY_3 - S_3 nU_3$	$nY_4 - S_4 nU_4$
nU_n	$-(nU_2) + \frac{nY_2}{F_2}$	$\frac{-(-D_3 - D_2)}{2S_2}$	$nU_2 + \frac{nY_3}{F_3}$	$nU_3 + \frac{nY_4}{F_4}$	
B_n, beam diameter	$2\max(\lvert pY_1\rvert, \lvert mY_1\rvert, \lvert nY_1\rvert)$	D_2	D_3	$2\max(\lvert pY_4\rvert, \lvert mY_4\rvert, \lvert nY_4\rvert)$	$2\max(\lvert pY_5\rvert, \lvert mY_5\rvert, \lvert nY_5\rvert)$
D_n'', min diameter	$\min(B_1, D_1)$	D_2	D_3	$\min(B_4, D_4)$	$\min(B_5, D_5)$
θ_n, angle of projection	$\arctan\frac{D_1''}{2S_1}$	$\arctan\frac{D_2''}{2S_2}$	$\arctan\frac{D_3''}{2S_3}$	$\arctan\frac{D_4''}{2S_4}$	
$\mathfrak{I}_n$, étendue	$\pi D_2^2 \sin^2\theta_1$	$\pi^2\frac{D_2^2}{4}\sin^2\theta_2$	$\pi^2\frac{D_4''^2}{4}\sin^2\theta_3$	$\pi^2\frac{D_4''^2}{4}\sin^2\theta_4$	
$\mathfrak{I}_{min}$, minimum étendue	$\min(\mathfrak{I}_1, \mathfrak{I}_2, \mathfrak{I}_3, \mathfrak{I}_4)$				

Table 3A. Layout for a spreadsheet to compute the geometrical optical properties of the sensor, an external source lens and a source.

element	detector	field_lens	collector	source lens	source
fl	n/a	0.2536	7.61	20	n/a
el_dia	0.07	0.198	2.65	20	10
dis_nx_el	0.201	7.61	1000	20	n/a
pY	-0.011848	0.099	1.325	-11.684198	-0.260184
pU	0.55148236	-0.1611038	0.0130092	-0.5712007	
mY	0.02314876	0.099	0	-13.009198	-0.260184
mU	0.37736935	0.0130092	0.0130092	-0.6374507	
nY	0.05814548	0.099	-1.325	-14.334198	-0.260184
nU	0.20325634	0.18712221	0.0130092	-0.7037007	
beam_dia	0.11629095	0.198	2.65	28.6683968	0.52036794
min_dia	0.07	0.198	2.65	20	0.52036794
theta	0.17240077	0.01300846	0.001325	0.46364761	
etendue	0.00362453	0.00293197	0.00173273	0.13362595	
min_etendue	0.00173273				

Table 3B. Numerical values for spreadsheet 3A.

A_4 is the image of A_2 created by the collector. If A_4 is smaller than the area of the field lens, A_{fl}, then,

$$P_{fl} = E_4 A_4 = L_1 \Omega_{A_2} A_4 \tag{21}$$

If A_4 is larger than the field lens, then,

$$P_{fl} = E_4 A_{fl} = L_1 \Omega_{A_2} A_{fl} \tag{22}$$

It can be seen that the maximum power collected is reached when $A_4 = A_{fl}$. Adding an additional lens in an attempt to focus more power in to the sensor is futile.

Table 3A shows the spreadsheet layout for sensor, the source lens and the source; table 3B shows the numerical results for typical values and figure 13 shows the ray trace. Not unexpectedly, while only a relative small source is needed, the source lens must be at least as large as the FOV. In this case, the beam diameter is limited to about 20 cm, much smaller than the required source lens of 28 cm. Tbe étendue is only $1.7X10^{-3}$. The next option is to magnify the sensor FOV.

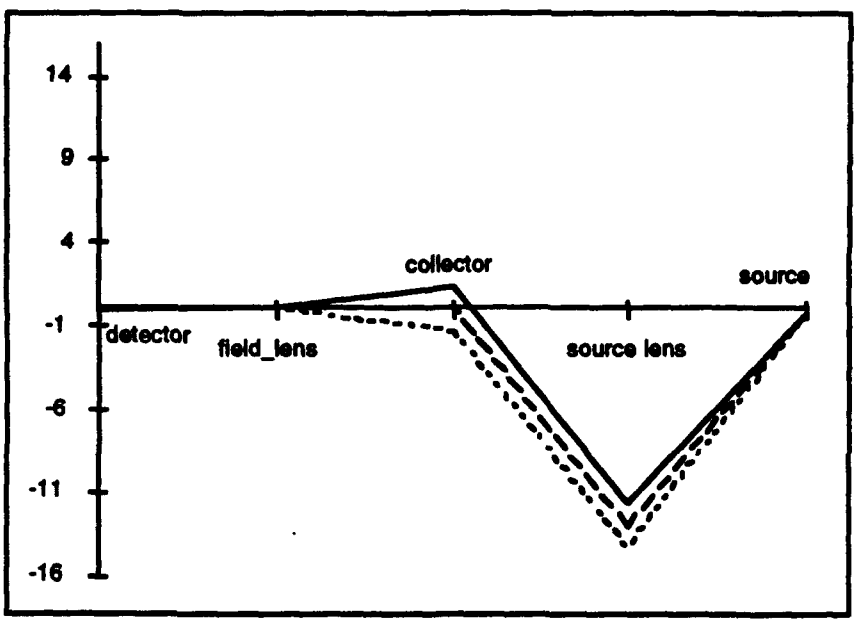

Figure 13. Ray trace for the collector, source lens and source

3.7 Magnifying the FOV

Remote sensors are designed to focus a distant source, i.e., accept parallel radiation from a distant extended source. If the source does not fill the FOV, then an external telescope can be placed in front of the sensor to magnify the source. The telescope would also allow the relatively close sources envisioned in this experiment to be collimated. A telescope consists of 2 lenses separated by a distance equal to the sum of their focal lengths for parallel incoming light. The first, or primary, lens focuses radiation from a distant object into an image located at its focal length. The second, or magnifier, lens collimates the beam again, but with a magnification, m, in the angle of divergence. See figure 14.

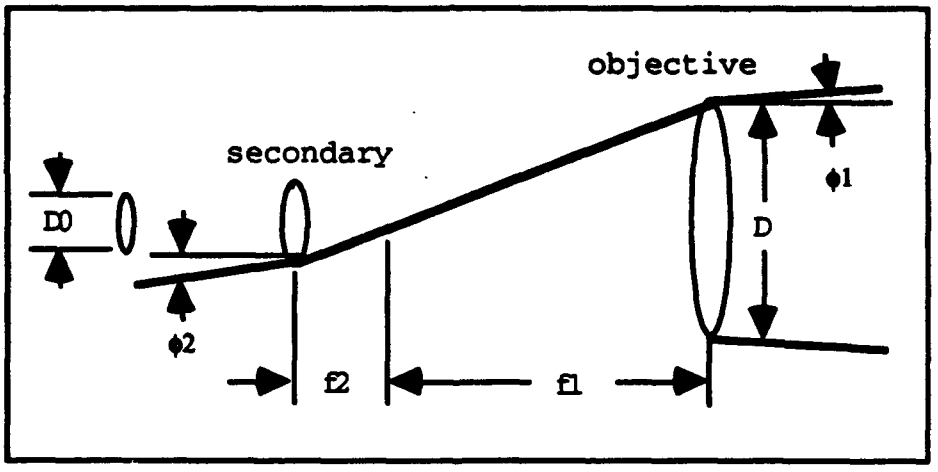

Figure 14: Function of a Telescope in Magnification of Object

The magnification of the telescope should be large enough that the source does fill the FOV. Magnification was defined in eq 13 as the ratio of image distance to object distance. It can also be defined as:

$$m = \frac{S'}{S} = \frac{f_1}{f_2} = \frac{\phi_2}{\phi_1} \qquad (23)$$

where f_1 is the focal length of the primary lens and f_2 is the focal length of the secondary lens; ϕ_2 is the angle of output ray and ϕ_1 is the

angle of the input ray. Note that the telescope takes a wide beam of low divergence and compresses it into a narrow beam of higher divergence. The sensor cannot usefully accept a ϕ_2 greater than the FOV, Θ; therefore, $\Theta = \phi_2$. Because of optical reciprocity we can look at the expanded image of the XM21 collector at the source distance to determine useful magnification. From inspection of figure 14, it can seen that the magnified diameter, D, of the beam is

$$D = mD_0 + \frac{S\Theta}{m} \tag{24}$$

where S is the range to the source from the telescope and D_0 is the diameter of the beam accepted by the XM21. Note that magnifying the source means increasing the diameter of the beam at the near and intermediate ranges; therefore, there is a possibility of over magnification. Correspondingly there should be an optimum magnification for any range that can be determined by differentiating the previous equation with respect to m, setting the result equal to 0 and solving for m. The result is

$$m = \sqrt{\frac{S\Theta}{D_0}} \tag{25}$$

Figure 15 shows magnification and lateral FOV as a function of range.

For S = 10 m the optimum magnification is about 3.2; the diameter of the unmagnified beam is 28.5 cm; the optimally magnified beam is 16.2 cm.

Because of the relatively close distance of the source, the telescope primary will bring the source to a focus at a slightly greater distance than the focal length. The secondary will have to be positioned such that the image falls at its focal length, so that the output beam is collimated and focused by the XM21 collector on the field lens. The separation, S_t, was computed from

$$S_i = f_2 + \frac{S f_1}{S - f_1} \qquad (26)$$

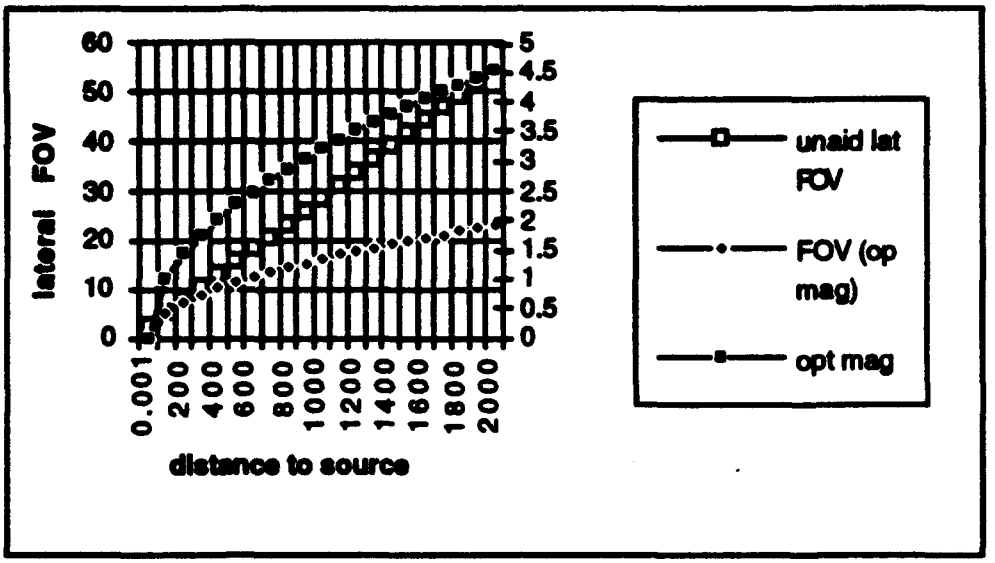

Figure 15. The left hand axis shows the lateral FOV for the unmagnified sensor and the optimally magnified sensor. The right hand axis shows the optimum magnification.

Next, consider matching the transfer of radiation between the secondary lens of the telescope and the XM21 collector. This can be viewed in several ways. The original XM21 was designed with a telescope. The secondary lens of the telescope was the same size as the XM21 collector and located about 20 cm from it. At such close ranges, the beam exiting the secondary should be almost completely intercepted by the collector. The étendue of such an arrangement is dependent on the actual separation of elements, but substantially higher value than necessary, about 0.01. Viewing the problem in a different way, i.e., that the secondary lens is a source for the collector, it is necessary and sufficient that the diverging beam of the secondary fill the aperture of the collector and that the secondary completely fill the FOV of the sensor.

Based on the need to fill the XM21 FOV, the minimum diameter of the secondary lens would be

$$D = 2S_u \tan\frac{\Theta}{2} \qquad (27)$$

where S_u is the separation between secondary and collector (needed to allow the insertion of beam splitters for multiple sensors. Figure 17 shows D as a function of S_u.

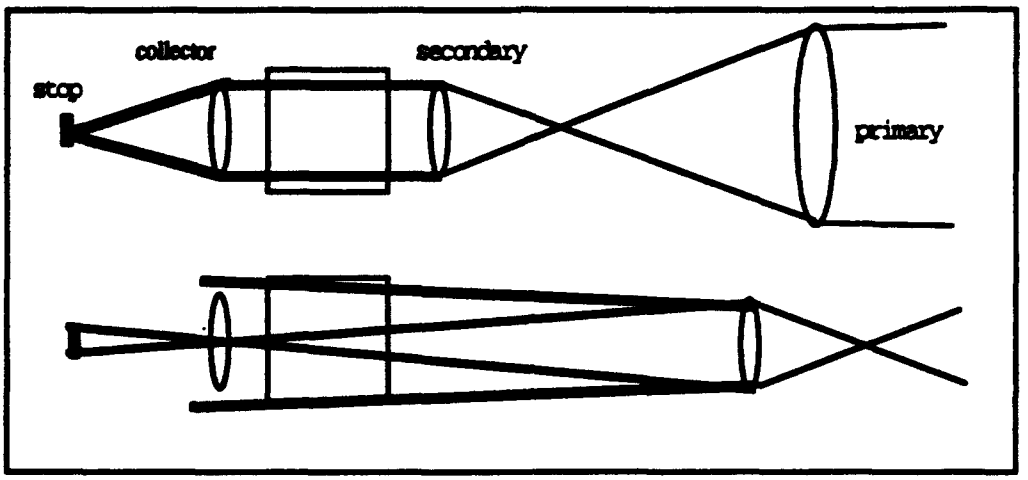

Figure 16. Two ways of looking at the transfer of radiation between the secondary of a telescope and the XM21 collector

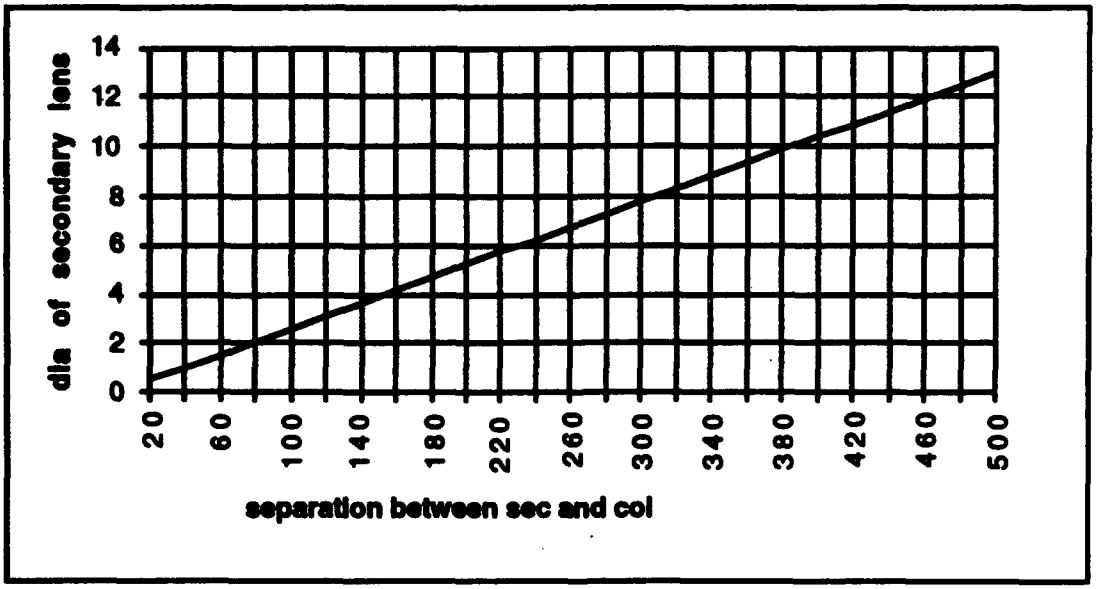

Figure 17. The diameter (cm) of the secondary lens needed to fill the FOV of the sensor as a function of separation between the secondary of the telescope and the collector of the sensor.

element, n	1, detector	2, field lens	3, collector	4, secondary	image	5, primary	6, source lens	7, source
F_n, focal length	n/a	F_2	F_3	F_4		F_5	F_6	n/a
Θ_n, element dia	D_1	D_2	D_3	D_4		D_5	D_6	D_7
S_n, dis next el	S_1	S_2	S_3	$F_4 + \frac{S_4 F_4}{S_4 - F_4}$		S_5	S_6	
pY_n	$pY_2 - S_1 pU_1$	$D_2/2$	$pY_2 - S_2 pU_2$	$pY_3 - S_3 pU_3$	$pY_4 - pU_4 F_4$	$pY_4 - S_4 pU_4$	$pY_5 - S_5 pU_5$	$pY_6 - S_6 pU_6$
pU_n	$-(pU_2) + \frac{pY_2}{F_2}$	$\frac{-(D_1 - D_2)}{2S_2}$	$pU_2 + \frac{pY_2}{F_2}$	$pU_3 + \frac{pY_3}{F_4}$		$pU_4 + \frac{pY_4}{F_5}$	$pU_5 + \frac{pY_5}{F_6}$	
mY_n	$mY_2 - S_1 mU_1$	$D_2/2$	$mY_2 - S_2 mU_2$	$mY_3 - S_3 mU_3$	$pY_4 - pU_4 F_4$	$mY_4 - S_4 mU_4$	$mY_5 - S_5 mU_5$	$mY_6 - S_6 mU_6$
mU_n	$-(mU_2) + \frac{mY_2}{F_2}$	$\frac{-(-D_2)}{2S_2}$	$mU_2 + \frac{mY_2}{F_2}$	$mU_3 + \frac{mY_3}{F_4}$		$mU_4 + \frac{mY_4}{F_5}$	$mU_5 + \frac{mY_5}{F_6}$	
nY_n	$nY_2 - S_1 nU_1$	$D_2/2$	$nY_2 - S_2 nU_2$	$nY_3 - S_3 nU_3$	$pY_4 - pU_4 F_4$	$nY_4 - S_4 nU_4$	$nY_5 - S_5 nU_5$	$nY_6 - S_6 nU_6$
nU_n	$-(nU_2) + \frac{nY_2}{F_2}$	$\frac{-(-D_2 - D_2)}{2S_2}$	$nU_2 + \frac{nY_2}{F_2}$	$nU_3 + \frac{nY_3}{F_4}$		$nU_4 + \frac{nY_4}{F_5}$	$nU_5 + \frac{nY_5}{F_6}$	
B_n, beam diameter	$2\max(\lvert pY_1\rvert,\lvert mY_1\rvert,\lvert nY_1\rvert)$	D_2	D_3	$2\max(\lvert pY_4\rvert,\lvert mY_4\rvert,\lvert nY_4\rvert)$		$2\max(\lvert pY_5\rvert,\lvert mY_5\rvert,\lvert nY_5\rvert)$	$2\max(\lvert pY_6\rvert,\lvert mY_6\rvert,\lvert nY_6\rvert)$	$2\max(\lvert pY_7\rvert,\lvert mY_7\rvert,\lvert nY_7\rvert)$
D_n*, min diameter	$\min(B_1, D_1)$	D_2	D_3	$\min(B_4, D_4)$	$2(pY_4 - pU_4 F_4)$	$\min(B_5, D_5)$	$\min(B_6, D_6)$	$\min(B_7, D_7)$
θ_n, angle of projection	$\arctan\frac{D_1^*}{2S_1}$	$\arctan\frac{D_2^*}{2S_2}$	$\arctan\frac{D_3^*}{2S_3}$	$\arctan\frac{D_4^*}{2F_4}$	$\arctan\frac{D_{4,5}^*}{2(S_4 - F_4)}$	$\arctan\frac{D_5^*}{2S_5}$	$\arctan\frac{D_6^*}{2S_6}$	
$\mathfrak{S}_n$, étendue	$\pi(D_1^*)^2 \sin^2\theta_1$	$\pi^2\frac{(D_2^*)^2}{4}\sin^2\theta_2$	$\pi^2\frac{(D_3^*)^2}{4}\sin^2\theta_3$	$\pi^2\frac{D_4^{*2}}{4}\sin^2\theta_4$	$\pi^2\frac{(D_{4,5}^*)^2}{4}\sin^2\theta_{4,5}'$	$\pi^2\frac{D_5^{*2}}{4}\sin^2\theta_5$	$\pi^2\frac{D_6^{*2}}{4}\sin^2\theta_6$	
$\mathfrak{S}_{min}$, minimum étendue	$\min(\mathfrak{S}_1,\mathfrak{S}_2,\mathfrak{S}_3,\mathfrak{S}_4,\mathfrak{S}_4',\mathfrak{S}_5,\mathfrak{S}_6)$							

Table 4A. Spreadsheet layout to compute the geometrical optical properties for the sensor, a telescope and a source lens. To get proper values of étendue for the telescope.

element	detector	field_lens	collector	secondary		primary	source lens	source	
fl	n/a	0.2536	7.61	6		24	20	n/a	
el_dia	0.07	0.198	2.65	6		24	10		1
dis_nx_el	0.201	7.61	100	30.5901639		1000	20	n/a	
pY	-0.011848	0.099	1.325	0.02408016	-0.0780552	-0.4966427	3.17424442	0.07341774	
pU	0.55148236	-0.1611038	0.0130092	0.01702256		-0.0036709	0.15504133		
mY	0.02314876	0.099	0	-1.3009198	-0.0780552	4.93368519	3.17424442	-0.0351888	
mU	0.37736935	0.0130092	0.0130092	-0.2038108		0.00175944	0.16047166		
nY	0.05814548	0.099	-1.325	-2.6259198	-0.0780552	10.3640131	3.17424442	-0.1437954	
nU	0.20325634	0.18712221	0.0130092	-0.4246441		0.00718977	0.16590199		
beam_dia	0.11629095	0.198	2.65	5.25183968		20.7280261	6.34848883	0.28759075	
min_dia	0.07	0.198	2.65	5.25183968	0.15611038	20.7280261	6.34848883	0.28759075	
theta	0.17240077	0.01300846	0.01324922	0.41253911	0.00317423	0.01036364	0.15739938		
etendue	0.00362453	0.00293197	0.01194588	0.00966618	0.01068149	0.01068045	0.00501425		
min_etendue	0.00293197								

Table 4B. Numerical values for 4A

Table 4 shows the spreadsheet layout for computing the étendue and ray trace for the telescopically aided sensor of m = 4. Up to this point the 'distance-to-the-next-element" was either fixed by the design or experimental constraints such as gas cell length. In the case of the separation of the secondary and the primary, eq 26 was inserted in the spreadsheet to compute the distance to the next element. This is the first occasion that a separation between 2 elements is computed. The ray trace in figure 18 shows a second consideration that we have chosen be taken into account. There is an image formed by the secondary lens at its focal point between itself and the primary. The beam then diverges to intercept the primary. Étendue was computed for these sections independently, although it does not necessarily have to be; because there is no limiting aperture at the image. The size of the image can be found by computing the height of the ray from the axis at focal point. This can be found from eq 10 where d'_n is the focal length. In the spreadsheet, only the ray height is computed at this point. Note in the ray trace, figure 18, a discontinuity appears at the image where the rays apparently change slope; this is not real. The apparent change is caused by the the limiited plotting capability.

At this point, it may be beneficial as a check to see a set of axial rays traced through the telescope. Replacing the diameter of the field lens, 0.198, with 0, the trace is redone to produce the results in figure 19, which are easily understood. Three rays from the center of the field lens are collimated by the collector and travel to the secondary, where they are brought to the focal point, diverge and are focused by the primary to a point on the center of the source lens. (The image is not shown as a separate element as it was in figure 18.) Only axial points are brought to these axial images. Even the modest displacement of 0.198/2 produces a displacement at the source lens of over 3 cm.

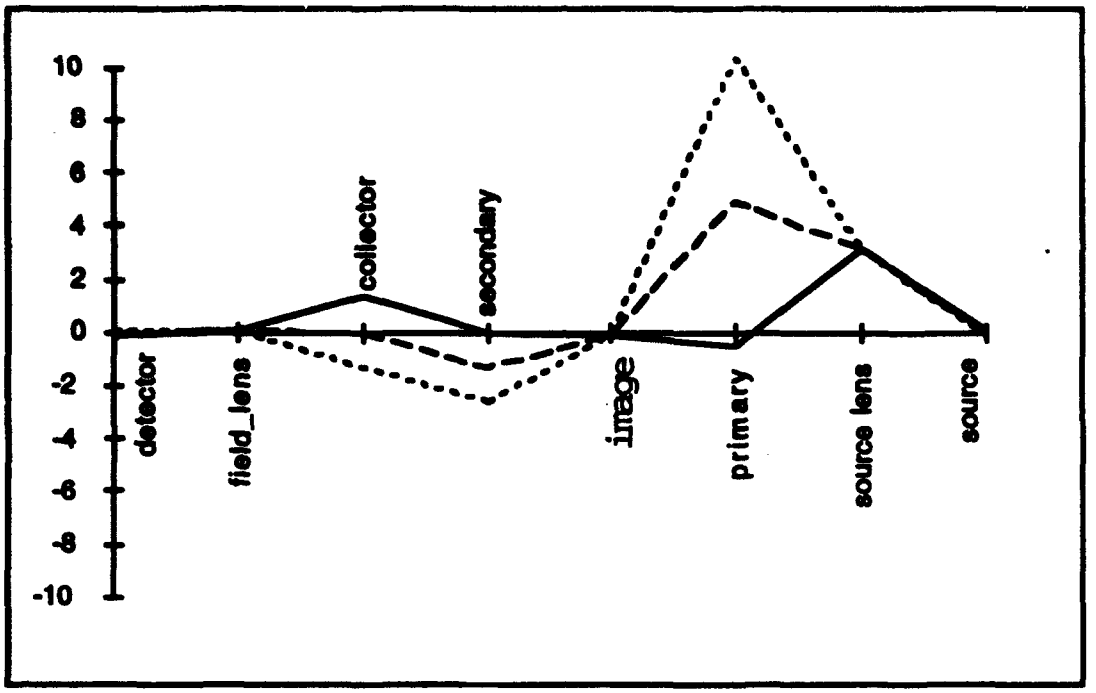

Figure 18. Ray trace of system described in table 4.

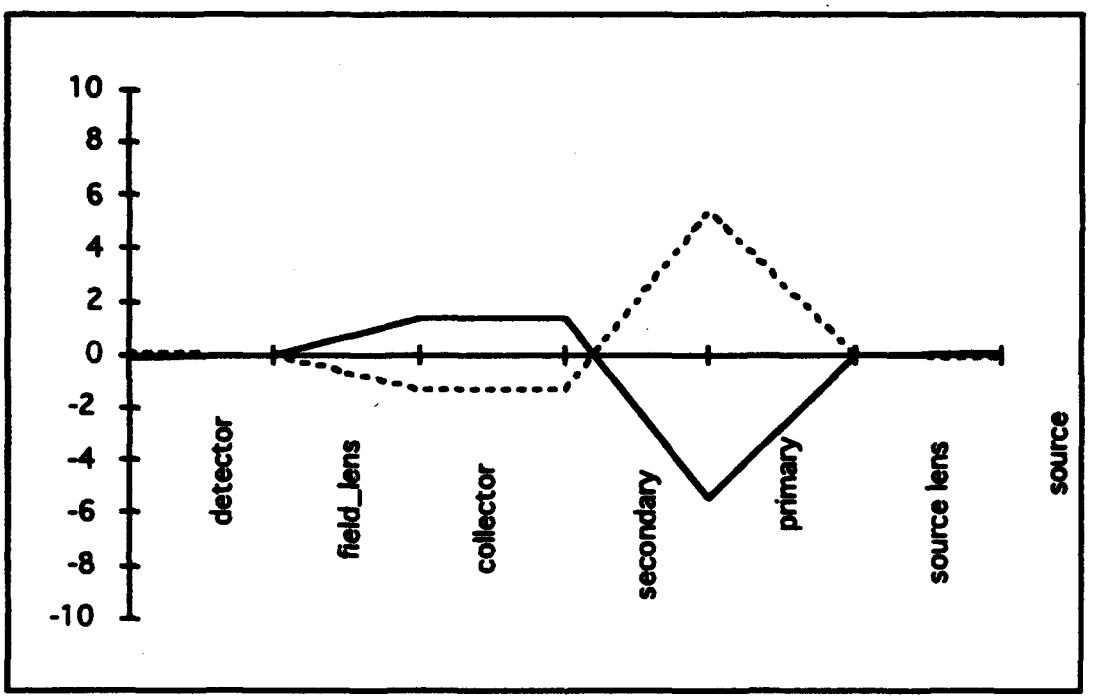

Figure 19. Trace of an axial point through the telescope.

3.8 Imaging the Source

Gladden and Marshall[2] proposed to use 2 long focal length lenses to focus the background source onto the collector of the XM21 sensor. The author criticised this design, because it delivered an image to the senor aperture, rather than a collimated beam. The analysis shows that the imaged beam is fuctionally equivalent to the collimated beam.

Marshall's design is shown in figure 20. These lenses are 15.2 cm (6 in) in diameter with focal lengths of 381 cm (150 in) with a spatial distribution as shown in the figure. The 3 lines of numbers directly below the schematic ray trace give his distances. Y = 10 is 1/2 the source diameter. The bottom 3 lines, in the figure, are the author's computations of the image distances for the 2 lenses, the magnification, and the image size. The second lens forms a virtual image 4191 cm behind itself, 120 cm in size. The first lens converts this in to a real image 410 cm in front of itself, 9.3 cm in size, almost a one to one size. The sensor is located 412 cm from lens 1.

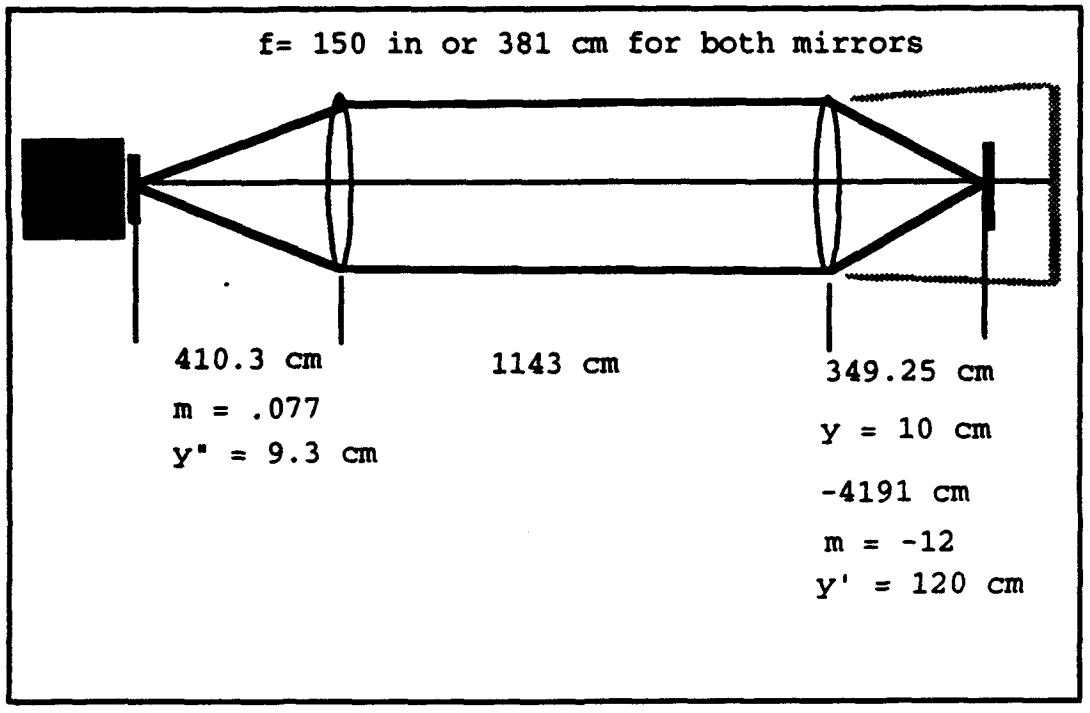

Figure 20. The 2 lens design by Marshall.

The design shown in figure 20 was further analyzed with the spreadsheet shown in table 5A. The lens 1 to lens 2 distance and the lens 2 to source distance were fixed. The collector to lens 1 distance was computed with a combined thin lens formula. Remembering that the rays are traced from left to right, but image distances were computed from right to left. The equation for computing the image formed by lens 2 is,

$$S' = \frac{S_5 F_5}{S_5 - F_5} \tag{28}$$

Substituting the results of this equation into an identical thin lens equation as the object distance, we have,

$$S' = \frac{F_4\left(S_4 - \frac{S_5 F_5}{S_5 - F_5}\right)}{S_4 - F_4 - \frac{S_5 F_5}{S_5 - F_5}} \tag{29}$$

This equation was inserted into the spreadsheet for the collector to lens 1 distance.

The numerical results are shown in table 5B and the ray trace is shown in figure 21. As with the telescopic design, lens 1 brings the collimated beam from the collector to a focus at its focal point. A column was inserted to allow the étendues to be independently calculated from lens 1 to image and from image to lens 2. This was done in the same way as for the telescopic design.

By comparing figures 18 and 21, there is one obvious difference between the telescopic system andd the 2 lens imaging system. For the telescopic system there is a one to one mapping between points on the source (the source lens in this case) and the field lens in the sensor, where the source is imaged. For the 2 lens system, the point in the image plane maps into many points in the source plane. The author can not think of any reason why that would invalidate the results for this experiment. For a multi-detector spectroradiometer this arrangement would be objectionable.

element, n	1, detector	2, field lens	3, collector	4, lens 1	image	5, lens 2	6, source
F_n, focal length	n/a	F_2	F_3	F_4		F_5	
D_n, element dia	D_1	D_2	D_3	D_4		D_5	D_6
S_n, dis next el	S_1	S_2	$\frac{F_4\left(S_4-\frac{S_3F_3}{S_3-F_3}\right)}{S_4-F_4-\frac{S_3F_3}{S_3-F_3}}$	S_4		S_5	
pY_n	$pY_2-S_1pU_1$	$D_2/2$	$pY_3-S_2pU_2$	$pY_3-S_3pU_3$	$pY_4-F_4pU_4$	$pY_4-S_4pU_4$	$pY_5-S_5pU_5$
pU_n	$-(pU_2)+\frac{pY_2}{F_2}$	$\frac{-(D_2-D_1)}{2S_2}$	$pU_2+\frac{pY_3}{F_3}$	$pU_3+\frac{pY_4}{F_4}$		$pU_4+\frac{pY_5}{F_5}$	
mY_n	$mY_2-S_1mU_1$	$D_2/2$	$mY_3-S_2mU_2$	$mY_3-S_3mU_3$	$pY_4-F_4pU_4$	$mY_4-S_4mU_4$	$mY_5-S_5mU_5$
mU_n	$-(mU_2)+\frac{mY_2}{F_2}$	$\frac{-(-D_1)}{2S_2}$	$mU_2+\frac{mY_3}{F_3}$	$mU_3+\frac{mY_4}{F_4}$		$mU_4+\frac{mY_5}{F_5}$	
nY_n	$nY_2-S_1nU_1$	$D_2/2$	$nY_3-S_2nU_2$	$nY_3-S_3nU_3$	$pY_4-F_4pU_4$	$nY_4-S_4nU_4$	$nY_5-S_5nU_5$
nU_n	$-(nU_2)+\frac{nY_2}{F_2}$	$\frac{-(-D_1-D_1)}{2S_2}$	$nU_2+\frac{nY_3}{F_3}$	$nU_3+\frac{nY_4}{F_4}$		$nU_4+\frac{nY_5}{F_5}$	
B_n, beam diameter	$2\max(\lvert pY_1\rvert,\lvert mY_1\rvert,\lvert nY_1\rvert)$	D_2	D_3	$2\max(\lvert pY_4\rvert,\lvert mY_4\rvert,\lvert nY_4\rvert)$		$2\max(\lvert pY_5\rvert,\lvert mY_5\rvert,\lvert nY_5\rvert)$	$2\max(\lvert pY_6\rvert,\lvert mY_6\rvert,\lvert nY_6\rvert)$
D_n^*, min diameter	$\min(B_1,D_1)$	D_2	D_3	$\min(B_4,D_4)$	$2(pY_4-F_4pU_4)$	$\min(B_5,D_5)$	$\min(B_6,D_6)$
θ_n, angle of projection	$\arctan\frac{D_1^*}{2S_1}$	$\arctan\frac{D_2^*}{2S_2}$	$\arctan\frac{D_3^*}{2S_3}$	$\arctan\frac{D_4^*}{2F_4}$	$\arctan\frac{D_{4,5}^*}{2(S_4-F_4)}$	$\arctan\frac{D_5^*}{2S_5}$	
$\mathfrak{S}_n$, étendue	$\pi D_1^2\sin^2\theta_1$	$\pi^2\frac{D_2^2}{4}\sin^2\theta_2$	$\pi^2\frac{D_3^{*2}}{4}\sin^2\theta_3$	$\pi^2\frac{D_{4,5}^{*2}}{4}\sin^2\theta_4$	$\pi^2\frac{D_5^{*2}}{4}\sin^2\theta_{4,5}$	$\pi^2\frac{D_5^{*2}}{4}\sin^2\theta_5$	
$\mathfrak{S}_{min}$, minimum étendue	$\min(\mathfrak{S}_1,\mathfrak{S}_2,\mathfrak{S}_3,\mathfrak{S}_4,\mathfrak{S}_5)$						

Table 5A. Ray trace for imaging the source onto the collector. The distance from element the sensor collector to the primary lens is chosen such that the source is imaged onto the collector.

element	detector	field_lens	collector	lens 1	image	lens 2	source
fl	n/a	0.534	7.61	381		381	n/a
el_dia	0.31	0.198	2.65	15.24		15.24	10
dis_nx_el	0.5743	7.61	410.307692	1143		349.25	n/a
pY	-0.0999933	0.099	1.325	-4.0127742	-4.9565046	-6.8439654	-1.4354167
pU	0.34649707	-0.1611038	0.0130092	0.00247698		-0.0154862	
mY	-1.657E-07	0.099	0	-5.3377742	-4.9565046	-4.1939654	8.8818E-16
mU	0.17238406	0.0130092	0.0130092	-0.0010007		-0.0120085	
nY	0.09999294	0.099	-1.325	-6.6627742	-4.9565046	-1.5439654	1.43541667
nU	-0.0017289	0.18712221	0.0130092	-0.0044784		-0.0085308	
beam_dia	0.19998653	0.198	2.65	13.3255484		13.6879309	2.87083333
min_dia	0.19998653	0.198	2.65	13.3255484		13.6879309	2.87083333
theta	0.17238518	0.01300846	0.00322927	0.01748581	0.00650451	0.01959367	
etendue	0.00362388	0.00293197	0.00456897	0.07412731	0.01025825	0.00780606	
min_etendue	0.00293197						

Table 5B. Numerical values for 5A.

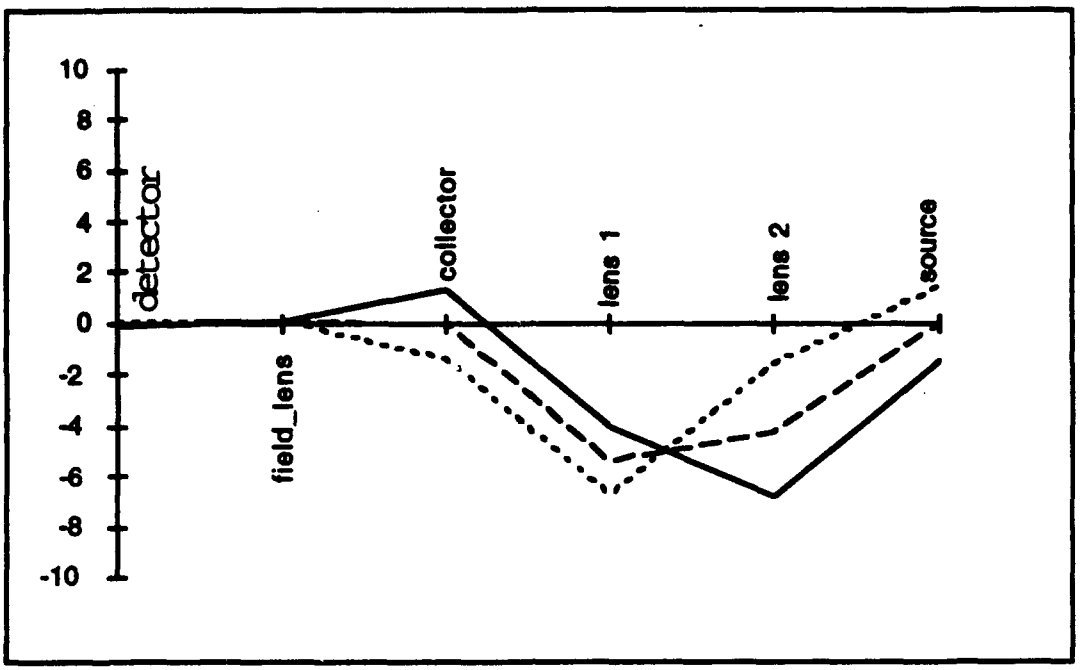

Figure 21. The graphical ray trace for table 5.

Experimentation with the lens-2-to-source distance showed that it changes both the required diameter of lenses 1 and 2 and the image distance from lens 1 to the collector; we found no critical dependencies. The spacings chosen by Marshall minimize the diameters of the 2 lenses; the active diameter is 13.7 cm; the actual diameter is 15.24 cm. The image distance from lens 1 to the collector can be changed by adding or subtracting to the lens-2-to-source distance. The active diameter of one or the other lens increased and the image distance changed. See table 6.

lens-2-to-source dis	-50	349.25	+50
lens-1-to-collector dis	448.3	410.3	361.8
active lens diameter	14.3	13.7	16.2

Table 6. Changes in image distance and active beam diameter for incremental changes of + and - 50 cm in lens-2-to-source distance.

In the +50 cm case, the diameter of the beam is larger than the 15.24 cm of the real lens.

4.0 Radiance

4.1 Total Power Law

The beam will encounter optical elements and gases in its traversal from source to detector. Each element will reflect, absorb and emit energy defined by[15]

$$\alpha+\rho+\tau=1 \qquad (30)$$

where α is the absorptance, ρ is the reflectance and τ is the transmittance.

First we apply the Total Power Law to optical elements. α is expected to be very small so that the element will not be a significant absorber or emitter; however, it may be necessary to keep lenses very clean for this condition to be maintained. The major source of loss for optical elements is expected to be reflection, but with antireflection coatings this may be as low as a few percent. Of course mirrors have high reflectance, but will have some very small losses from absorption or scattering. Beam splitters have also been proposed in order to test several sensors simultaneously with coincident optical paths. Beam splitters are normally designed to transmit 50% and reflect 50% of the beam. If several splitters are used in series the resulting loss will be 75% of the incident beam, a loss which must be offset by increasing the source radiance, i.e. increasing the source temperature.

There is another very important effect: A beam splitter creates 2 lines-of-sight (LOS): generally the LOS of the experiment and an alternate LOS orthogonal to the planned LOS. The beam splitter not only reduces the signal from the planned source; it adds radiation from the external environment along the orthogonal LOS. That may be warm instruments, people walking around the room, or the sides of other sensors. In fact, these environmental influences are likely to project more radiation into the XM21's than the gas and background sources, because the radiation from the latter source is attenuated by all of the optics within the train. In an

incandescent source experiment, these contributions may be insignificant; in the world of thermal infrared, they are bound to be of significance. One solution is to block the orthogonal path of each beam splitter with a cooled baffle.

Next, the Total Power law is applied to the gas contained in the sample cell. Scattering is expected to be negligible. The Total Power Law is

$$\alpha + \tau = 1 \tag{31}$$

Equation 31, for a homogeneous volume of gas, at a single optical frequency, υ, translates to[16]

$$L = (1 - e^{-acl})L_g + e^{-acl}L_{bg} \tag{32}$$

where the first term in brackets on the right is the emittance term and the second is the transmittance of the background radiance. L_g is the radiance of a blackbody at the temperature of the gas and L_{bg} is the radiance of the background reference source diminished by the intervening optics. a is the absorption coefficient of the gas at some wavenumber, cl is the concentration pathlength product usually in mg/cm^2.

Blackbody radiance can be computed from

$$L = \frac{2h}{c^2}\frac{\bar{\nu}^3 d\upsilon}{e^{h\nu/kT} - 1} = \frac{c_1 \bar{\nu}^3 d\upsilon}{e^{c_2\bar{\nu}/T} - 1} \tag{33}$$

where $c_1 = 1.19089 \times 10^{-12}$, and $c_2 = 1.4388$. $\bar{\nu}$ is the wavenumber, cm^{-1}, and T is the temperature in °K. Equation 33 can be solved for temperature.

$$T = \frac{c_2 \nu}{\ln\left(\frac{c_1 \nu^3 d\nu}{L} + 1\right)} \tag{34}$$

4.2 Delta Temperature

The definition of ΔT needs clarification; it is defined as the difference between the radiometric temperature of the background and the temperature of the air mass containing the chemical target gas.[17] For these experiments, it is defined as the difference between the blackbody reference source and the air in the gas cell. These definitions are easily understood, however, the sensor sees ΔT, the temperature contrast, as a spectral contrast. In regions of strong bands, the radiance will be more heavily weighted in favor of the temperature of the gas cloud; in regions of low spectral activity the radiance will more accurately be a measure of the background temperature. Furthermore, the gas will be seen as absorber against a hotter background reference source or an emitter against a colder reference source. From this, we can see that temperature contrast is not an absolute thing; it varies continuously and with changing polarity in spectral regions where the target gas has spectral bands. Because the instrument responds to spectral contrast, the ΔT is defined, or more fundamentally, ΔL, as the contrast between 2 spectral band; one of strong absorption, the analytical band, and one with very low absorption, the reference band.

$$\Delta L = L_R - L_A \tag{35}$$

There have been questions raised about possible distortion caused by raising the temperature of the background source because the elevation is not uniform at all optical frequencies. Figure 22 shows the radiance difference between a 300°K blackbody and blackbodies at various ΔT's. There is some distortion of the spectrum. Taking the ratio of the positive ΔT's and then the negative ΔT's, there is about 6 to 13% more or less energy between the extreme ends of the spectrum. This is probably not a significant distortion given the other variables of the problem. It is, however, beyond the limits of this study.

As stated in the goals, the objective is to compute the signal in various configurations of external optics and source and gas temperatures difference power received from the difference radiance, ΔL, is

$$\Delta P = \Im_m \Delta L = \Im_m (L_R - L_A) \tag{36}$$

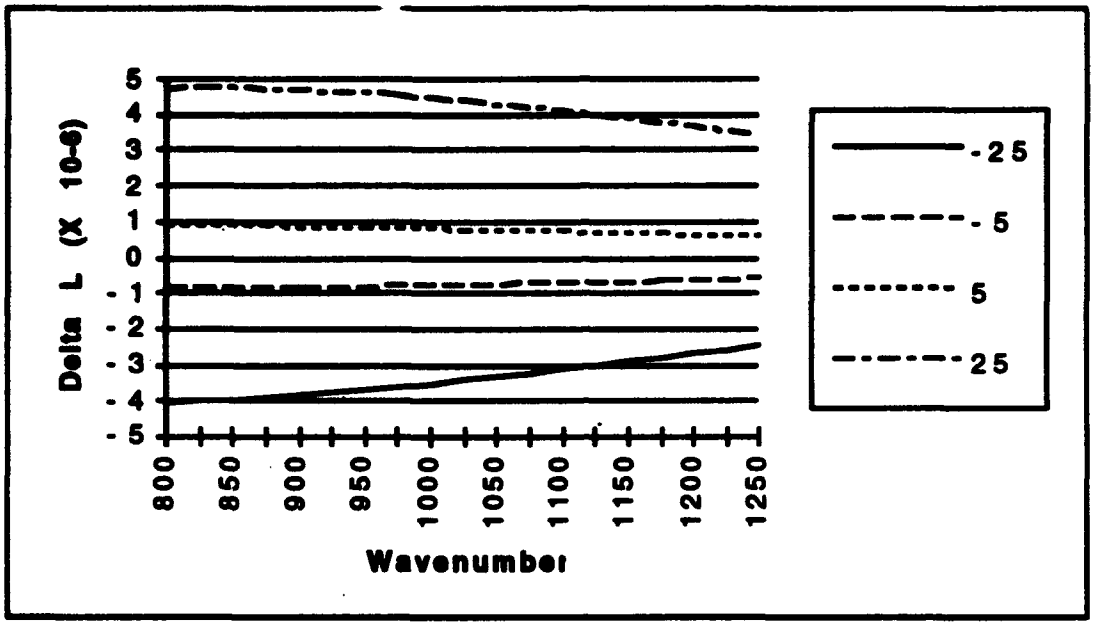

Figure 22. The ΔL's associated with ΔT's in the legend. The spectral range is 800 to 1250 cm^{-1}, about the range of the XM21.

4.3 The Gas Cell

The first configuration that will be examined is the source that completely fills the XM21 FOV; i.e., the sensor étendue is the limiting étendue. The only intervening optics are the gas cell windows. From inspection of figure 23 and eq 32 and basic radiative transfer theory, the radiance exiting the gas cell at optical frequency, $\bar{\nu}$, is

$$L_\nu = \tau_w (1 - \tau_g) L_g + \tau_w^2 \tau_g L_{bg} \tag{37}$$

where τ_W is the window transmittance, L_g is the radiance of a blackbody at the temperature of the gas and L_{bg} is the radiance of a blackbody at the background source temperature.

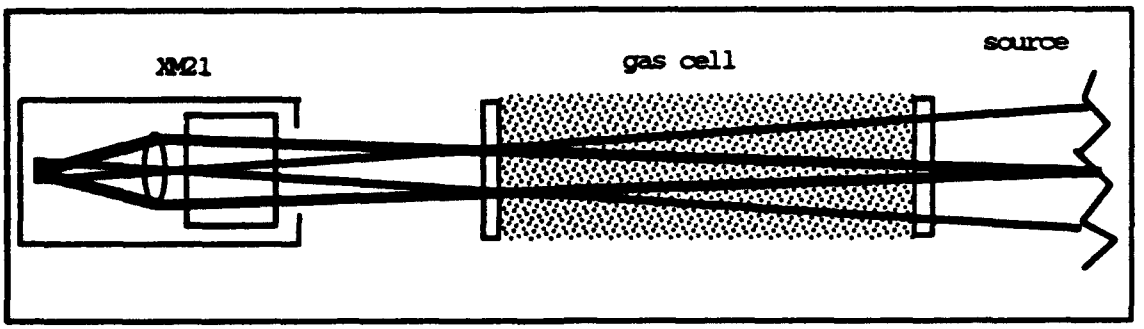

Figure 23. The simplest possible arrangement. The gas cell may or may not have windows. Each point on the source emits a wave that each least fills the entrance aperture of the sensor and the source at least fills the FOV of the sensor.

Assume that the emissivity of the reference source is 1. The transmittance of the gas at the analytical and reference frequencies is respectively

$$\tau_A = e^{-\alpha_A cl}$$
$$\tau_R = e^{-\alpha_R cl} \qquad (38)$$

Rewriting eq 36

$$\Delta P = \Im_m (L_A - L_R)$$

L_A and L_R are computed at different optical frequencies; we will assume that they are sufficiently close that a single average frequency can be used to compute ΔP and the required background blackbody temperature.

$$\Delta P = \Im_m [\tau_w (1-\tau_A) L_g + \tau_w^2 \tau_R L_{bg} - \tau_w (1-\tau_R) L_g - \tau_w^2 \tau_R L_{bg}]$$
$$\Delta P = \Im_m [\tau_w (\tau_R - \tau_A) L_g + \tau_w^2 (\tau_A - \tau_R) L_{bg}] \qquad (39)$$
$$\Delta P = \Im_m (\tau_R - \tau_A)(\tau_w^2 L_{bg} - \tau_w L_g)$$

Eq 39 can be used to compute ΔP received from analytical and reference frequencies. The radiances L_g and L_{bg} can be computed from eq 33 for blackbodies at the gas temperature, T_g and the background blackbody

temperature, T_{bg}. Assuming no optical elements other than the sensor, the expected power difference will be computed for a range of ΔT's. From these values, the background blackbody temperature can be computed that is required to offset the losses caused by the optical elements, if we assume that the gas temperature remains constant. Solving eq 37 for the temperature of the blackbody source

$$T_{bg} = \frac{c_2 \bar{\nu}}{\ln\left[\dfrac{c_1 \bar{\nu}^3}{\dfrac{\Delta P}{\Im_m \tau_w^2 (T_R - T_A)} + \dfrac{L_g}{\tau_w}} + 1\right]} \qquad (40)$$

Equations 33, 39 and 40 were programmed into one row of a spreadsheet to compute required background blackbody temperature for a specified ΔT. The calculation can be repeated for other ΔT's by duplicating the calculations in the following rows. See table 7.

	L_{bg} w/o windows	ΔP at the sensor	T_{bg} required to offset window loss
ΔT	$\dfrac{c_1 \bar{\nu}^3}{e^{c_2 \bar{\nu}/T_g + \Delta T} - 1}$	$\Im_m (\tau_R - \tau_A)(\tau_w^2 L_{bg} - \tau_w L_g)$	$\dfrac{c_2 \bar{\nu}}{\ln\left[\dfrac{\varepsilon c_1 \bar{\nu}^3}{\dfrac{\Delta P}{\Im_s \tau_w^2 (T_R - T_A)} + \dfrac{L_{gas}}{\tau_w}} + 1\right]}$

Table 7. One row of a spreadsheet to calculate the reference blackbody temperature to off window losses.

Table 8 shows the actual results of a complete spreadsheet for configuration 1.

Inspection of the last column (T req w/win) shows an unexpected result: the required temperatures are offset about 3° in the plus direction. After consideration, it seems likely that the optics between the gas and the background source produce the offset. It was fully expected that the optics would reduce the effective signal, consequently

would require the reference source temperature increment, either plus or minus, to be increased, but the offset was unexpected. When the window transmittance was set to 1, the offset disappeared and the required background source temperature was exactly what was required to meet the specified ΔT. This can be checked by putting both windows outside both the gas cell and the reference source. See figure 24.

cl	90			
	a, abs coeff	trans		
anal band	1.46E-03	0.87686696		
ref band	1.43E-05	0.99871383		
win trans	0.95			
gas cell temp	300			
anal opt freq	1020			
ref opt freq	1020			
avg opt freq	1020			
L(bb) at gas cell temp	9.559E-06			
	spec Del T	L w/o win	Del P	T req w/win
	-5	8.7931E-06	-2.545E-10	297.775429
	-4	8.9432E-06	-2.046E-10	298.85226
	-3	9.0948E-06	-1.543E-10	299.928534
	-2	9.248E-06	-1.034E-10	301.004268
	-1	9.4027E-06	-5.193E-11	302.07948
	0	9.559E-06	0	303.154185
	1	9.7168E-06	5.245E-11	304.228401
	2	9.8762E-06	1.0542E-10	305.302142
	3	1.0037E-05	1.589E-10	306.375423
	4	1.02E-05	2.129E-10	307.448258
	5	1.0364E-05	2.6742E-10	308.520663

Table 8 . Results of spreadsheet computation for a gas cell with windows.

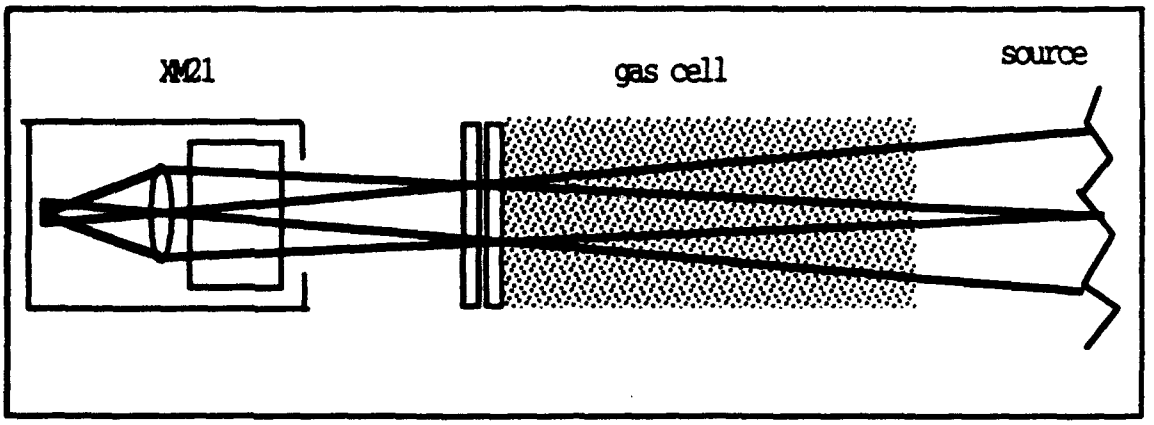

Figure 24. A modification of configuration 1 to check the effect of window position on the ΔT offset.

Solving eq 37 for T_{bg} in the new configuration.

$$T_{bg} = \frac{c_2 \upsilon}{\ln\left[\dfrac{\dfrac{\varepsilon c_1 \upsilon^3}{\Delta P}+1}{\dfrac{\Im_s \tau_w^2 (T_R - T_A)}{L_g}}\right]} \qquad (41)$$

When the results from this equation are plotted beside those from the original equation for the same conditions, the offset no longer occurs when both windows are on one side of the cell. See figure 25.

4.4 Meso- and Ecto-Optics

Figure 25 shows that the position of the windows is important to the source temperature. Generalizing these observations, all of the optical elements between the background source and the gas source produce an offset effect as well as an attenuation. These will be referred to as the meso-optics. Optics outside both sources produce attenuation only. These will be referred to as the ecto-optics. See figure 26.

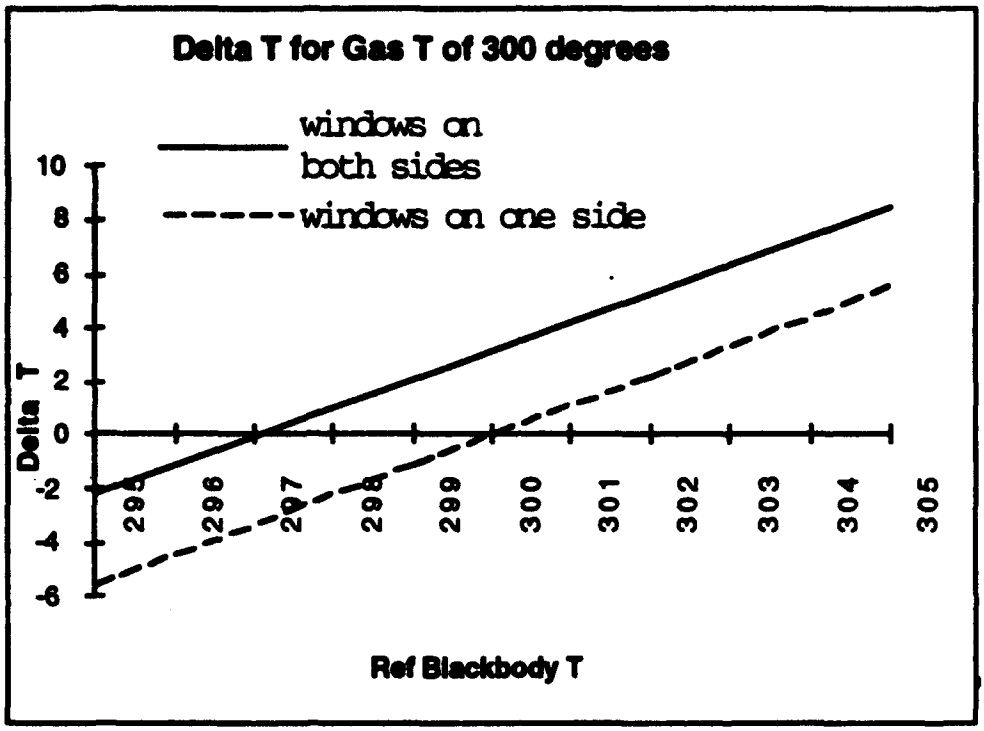

Figure 25. The difference between the required background temperature when the windows bound the gas and when the windows are on the outside of the gas.

The total transmittance of the meso-optics, is

$$\tau_{mo} = \prod_{i=1}^{m} \tau_i \tag{42}$$

where m is the number of optical elements between the background source and the gas. The transmittance of the ecto-optics is

$$\tau_{eo} = \prod_{j=1}^{n} \tau_j \tag{43}$$

where n is the number of exterior optical elements.

Reformulating eq 37

$$L_v = \tau_{eo}[(1-\tau_g)L_g + \tau_{mo}\tau_g L_{bg}] \tag{44}$$

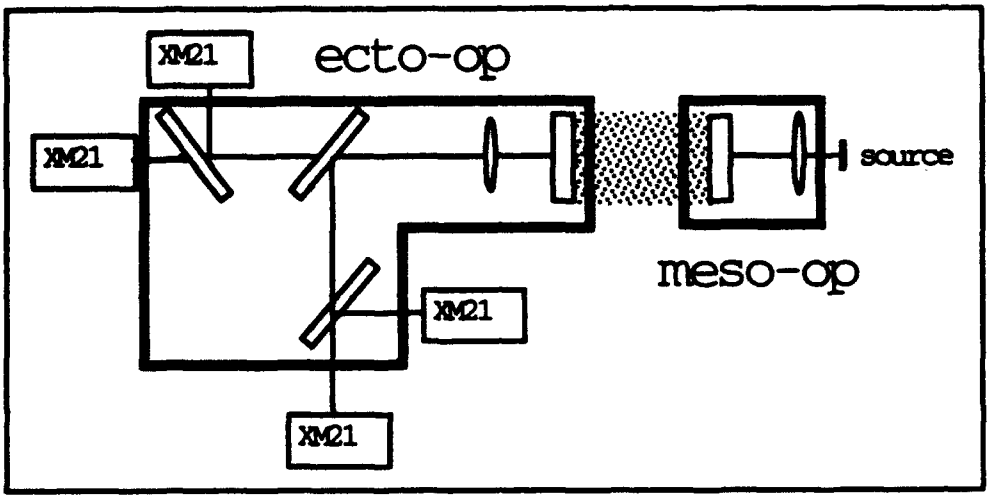

Figure 26. Definition of meso- and ecto-optics.

The difference power equation is

$$\Delta P = \Im \Delta L = \Im \tau_{eo}(\tau_R - \tau_A)(\tau_{mo} L_{bg} - L_g) \quad (45)$$

Solving for T_{bg}

$$T_{bg} = \frac{c_2 \bar{v}}{\ln\left[\frac{c_1 \bar{v}^3}{\frac{1}{\tau_{mo}}\left(\frac{\Delta P}{\Im_s \tau_{eo}(\tau_R - \tau_A)} + L_g\right)} + 1\right]} \quad (45)$$

Using this equation we will investigate the behavior of meso and ecto-optics in more detail. Figure 27 shows required background source temperature needed to maintain ΔT, when the gas temperature is 300°for 3 cases: 1) without windows, 2) $\tau_{eo} = .95, and\ \tau_{mo} = 1$, and 3) $\tau_{mo} = .95, and\ \tau_{eo} = 1$. As can be seen, the required background temperature for both no-windows and ecto-windows nearly overlaps; the meso-optics case is displaced by an almost constant 3°.

Figure 28 shows the required ΔT that T_{bg} must be maintained above T_g to maintain an apparent $\Delta T = 0$ as a function of meso-optics transmittance. Values of transmittance were estimated for the configuration shown in figure 1. The background source ΔT required to maintain a specified ΔT to the sensor is shown in figure 29. The offset at 0° is + 4.3°.

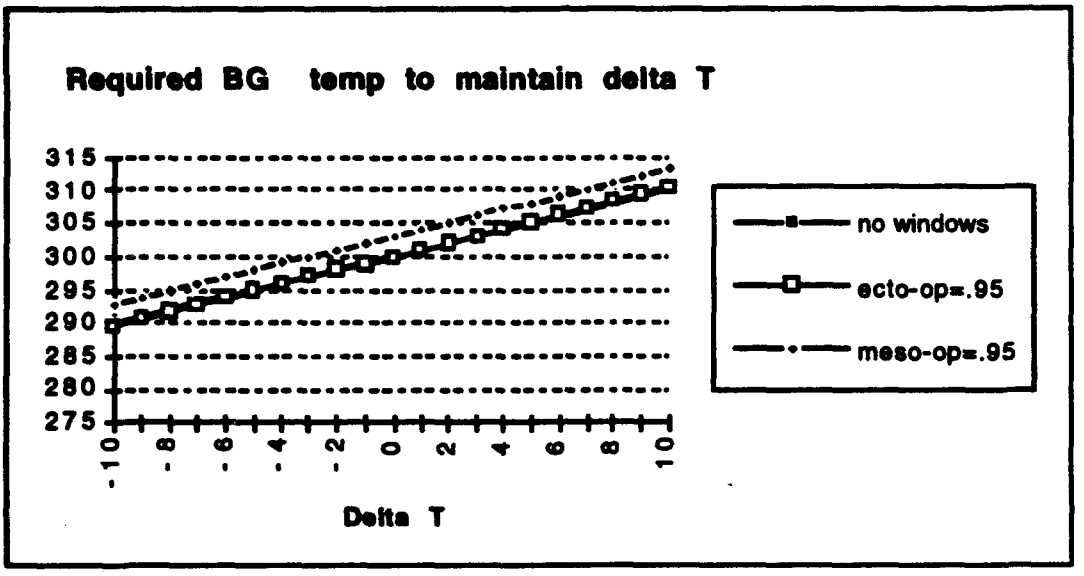

Figure 27. The required background source temperature to maintain a specified ΔT for: 1) no windows, 2) meso-optics = .95, ecto-optics = 1, 3) ecto-optics = .95, meso-optics = 1.

5.0 Summary

The various factors inherent in delivering a beam of specified radiance to the sensor include: the geometrical factors needed to assure that the background source fills the field-of-view, methods of multisensor viewing and the effects of the transmittance of the additional optical elements. Source optics, short range telescopes, imaging optics, optical transmittance and element position were analyzed. Several optical configurations will deliver a suitable beam. The telescopically based system delivers a spatially similar beam to what the sensor would see in the field. It may be more flexible in handling range effects. However, it is more complex and may require a wider cell. The 2 lens system that delivers an image at the entrance aperture does deliver a beam, that is

functionally equivalent to a collimated beam at least for single detector spectroradiometers. Its apparent disadvantages are: it would not deliver a suitable beam determining spatial effects with multi-detector spectroradioometers and it may be less flexible in handling range variations. The radiance analysis showed that the position of the optical elements is important. Elements between the background source and the gas cell (meso-optics) have different effects from elements outside both sources (ecto-optics).

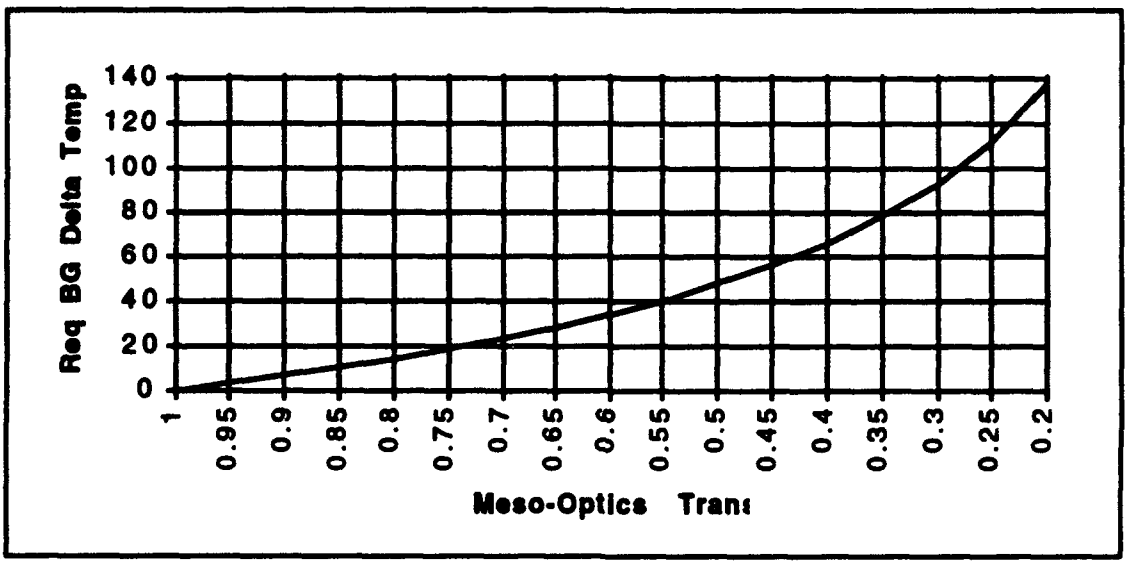

Figure 28. The required ΔT that T_{bg} must be maintained above T_g to maintain an apparent $\Delta T = 0$ as a function of meso-optic transmittance.

6.0 Recommendations

Over the years of testing standoff sensors with gas cells, there has been considerable discussion about distortion of data by cell windows. However ,windowless gas cells are difficult to control. These results, if experimentally verified, suggest that there is very little penalty to a one window cell, which might be substantially easier to design and build. Even reference source temperature corrections for a 2 window cell may be considerably easier to implement than a one window cell. These results apply to windows with reflection losses only. The analysis of absorbing elements was not attempted in this investigation.

In past XM21 tests, cells with windows were used. Typical reference source temperatures have been +5°C, but according to recent workers, no allowances were made for window reflection losses in the data analysis. For window losses as little as 5%, the actual ΔT would have been 1 to 2°C.

This effort has been completely analytical; experimental verification is planned for the coming year.

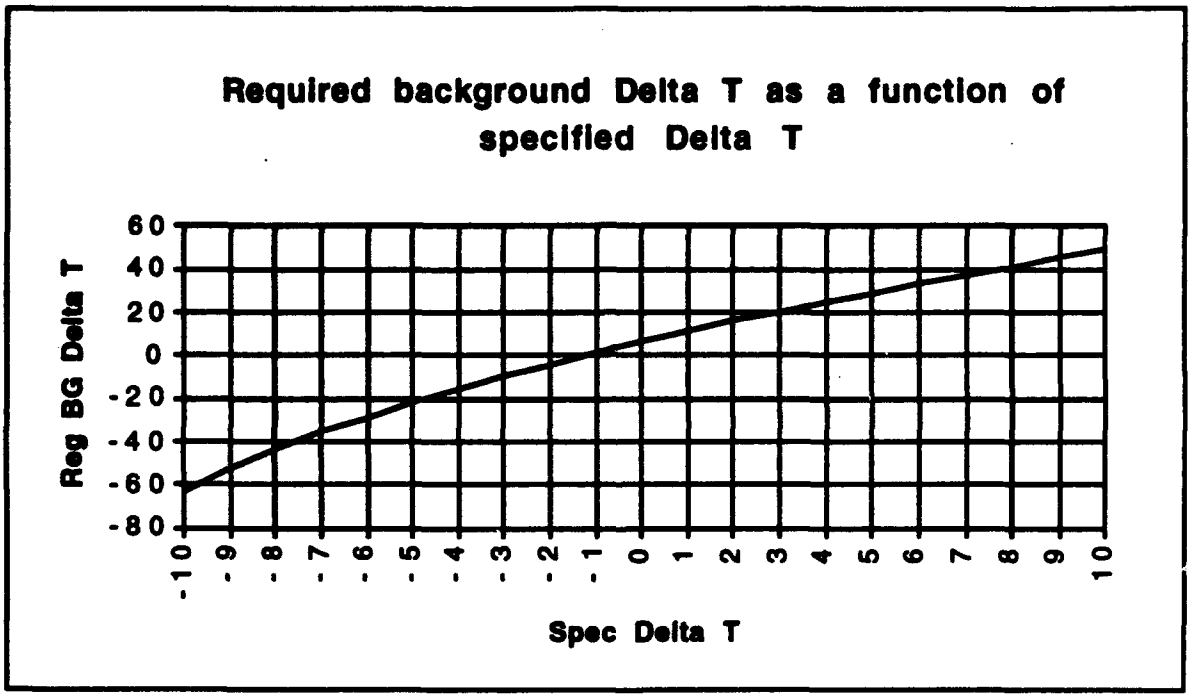

Figure 29. Required background ΔT to compensate for losses incurred by the optics shown in figure 1.

References

[1] CRDEC-SP-041,Root Cause Analysis, Steady State Alarm and Consistent Performance Problems, XM21 Remote Sensing Chemical Agent Alarm, D.C.Shandle, R.G. Roux, W.C. Hanger, V.J. Cannaliao, M.C. Miller, Jan 1992.

[2] Methodology Study Report for the XM21 Remote Sensing Chemical Agent Alarm (RSCAAL) Risk Reduction Program (RRP), Volume I, David J Gladden, February 1993.

[3] F.E. Nicodemus, Radiance, Am J. Physics, 31, 368, (1963)

[4] Wyatt, Clair L., Radiometric Caliibration, pg 43, Academic Press, 111 Fifth Ave, New York, NY, (1978)

[5] Ref 4, pg 25

[6] Reinhard Beer, Remote Sensing By Fourier Transform Spectrometry, pg 15, John Wiley & Sons, Inc, (1992)

[7] John Strong, Concepts of Classical Optics, pg 342, W.H. Freeman & Co, (1958)

[8] The Infrared Handbook, Chapter 8, Optical Design, W. J. Smith, pg 8-13, ERIM, ed by Wolfe and Zissis, 3rd edition.

[9] Technical Data Package for the XM21 Remote Sensing Chemical Agent Alarm, PM-NBC Defense, POC: David Foster, 410-671-6524

[10] XM21 Design Status Review, 12, 13 May 1982, Honeywell Inc, Electro-Optics Operation.

[11] The function of field lens are described in ref 7, Chapter 9, pg 9-9, W. J. Smith.

[12] The Infrared Handbook, page 8-9, equation 8-7

[13] OSA Handbook of Optics, page 7-93, ed by Driscoll and Vaughan, McGraw-Hill, (1978)

[14] OSA Handbook of Optics, page 7-71

[15] The Infrared Handbook, page 7-29, W. L. Wolfe

[16] D. F. Flanigan and H. Walter, The Computer Simulation and Optimization of Passive LOPAIR, appendix, ED-TR-74070, (1975)

[17] D. F. Flanigan, Detection of Organic Vapors with Active and Passive Sensors: A Comparison, Apl Opt, 25, 4253, (1986)

Blank

APPENDIX

XM21 SPECIFICATIONS

SYSTEM SPECIFICATIONS

PARAMETER	REQUIRED	PROJECTED	MARGIN
NESR (W/cm^2-sr-cm^{-1}) (1 s INTEGRATION @ 1000 cm^{-1})	1.2×10^{-9}	7.8×10^{-10}	37%
SPECTRAL RANGE (cm^{-1}) (1/3 RESPONSE POINTS)	1200-833	1270-760	5 - 10%
RESOLUTION (cm^{-1}) (TRIANGULAR APODIZATION)	4	3.5	12%
SCAN TIME (s)	0.13	0.105	19%
FIELD-OF-VIEW (DEGREES)	1.5 x 1.5	1.5 x 1.5	--

NESR

$$NESR = \sqrt{A_D} / \Theta \eta_v \Delta\nu \sqrt{T} K D^*_{\lambda p}$$

A_D = DETECTOR AREA (cm^2) = $(0.07\ cm)^2 = 0.005\ cm^2$

Θ = THROUGHPUT (cm^2-sr) = $\pi/4\ (2.54\ cm)^2 \times (1.5°)^2 (0.0175\ r/°)^2 = 3.5 \times 10^{-3}\ cm^2$-sr

η_v = EFFICIENCY = 0.26 (OPTICS) x 0.8 (MODULATION EFFICIENCY) = 0.21

$\Delta\nu$ = RESOLUTION (cm^{-1}) = 4 cm^{-1}

T = INTEGRATION TIME (s) = 1 s

K = APODIZATION WEIGHING FUNCTION = 0.87

$D^*_{\lambda p}$ = PEAK DETECTIVITY ($cm\sqrt{Hz}/W$) = 3.5×10^{10} $cm\sqrt{Hz}/W$ @ 10 µm

$$NESR = 7.8 \times 10^{-10}\ W/cm^2\text{-sr-}cm^{-1}$$

APPENDIX

XM21 SPECIFICATIONS

SPECIFICATIONS

SIZE: 0.027 IN. x 0.027 IN. $^{+0.002}_{-0.000}$ IN.

OPERATING MODE: PHOTOCONDUCTIVE

SPECTRAL RANGE: 60% RESPONSE AT 8 μm
50% RESPONSE AT 12 μm

OPERATING TEMPERATURE: 80 K NOMINAL

RESISTANCE: 10 Ω < R_D < 60 Ω

DEWAR HEAT LOAD: 0.250 W MAXIMUM, WHEN STORED AND OPERATED UNDER THE SPECIFIED CONDITIONS, FOR A PERIOD OF 2 YEARS

SPECIFIC DETECTIVITY:
$D^*(\lambda_{PK}, 1\ kHz, 1\ Hz, 60°) \geq$
3.5×10^{10} cm-$Hz^{1/2}$/W
WHERE $D^*_\lambda \times 0.7 = D^*_\lambda$ MEASURED.*

RESPONSIVITY: $R_{\lambda_P} \geq 200$ V/W
WHERE $R_{\lambda_{PK}} \times 0.7 = R_{\lambda_{PK}}$ MEASURED*

* ASSUMES WINDOW TRANSMITTANCE OF 70%

IMAGE QUALITY:
SYSTEM RESPONSE AT THE EDGE OF THE FIELD

90% SLIT WIDTH: 0.17°
THREE COLORS: 8, 10, 12 μm, EQUALLY WEIGHTED INCLUDING DIFFRACTION.

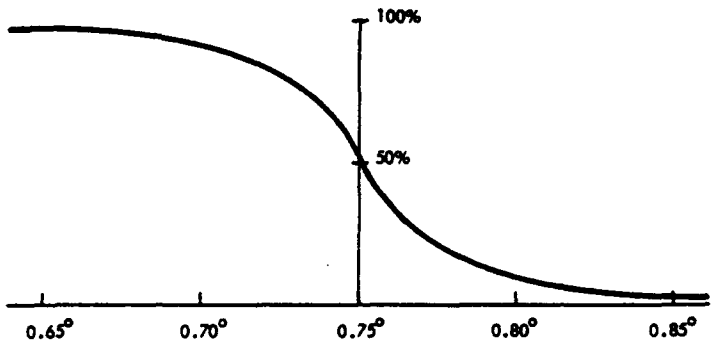

APPENDIX

XM21 SPECIFICATIONS

XM21 SYSTEM

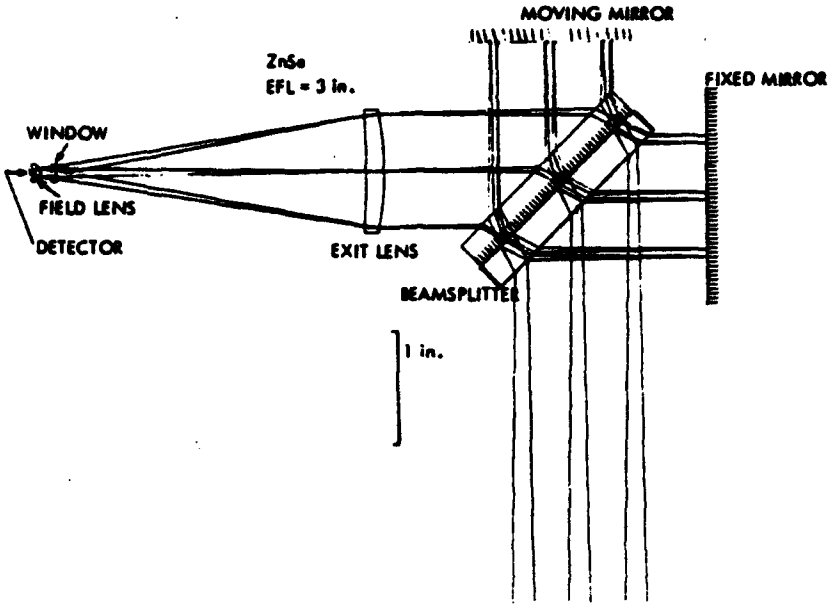

XM21 DETECTOR LENS

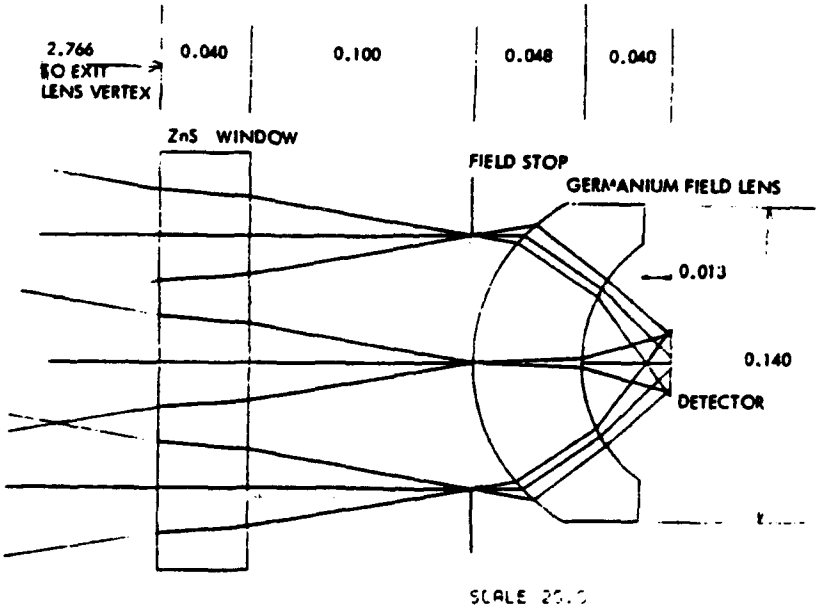

SCALE 25:1

APPENDIX

XM21 SPECIFICATIONS

OPTICAL ELEMENT TRANSMITTANCES/REFLECTANCES

ELEMENT	MATERIAL	TRANSMISSION	REFLECTION
MOVING MIRROR	Al	-	0.94
FIXED MIRROR	Al	-	0.94
EXIT LENS	ZnSe	0.96	-
DEWAR WINDOW	ZnS	0.72*	-
FIELD LENS	Ge	0.96	-

*UNCOATED ZnS TO ALLOW FUSING TO DEWAR GLASS

XM21 PRESCRIPTION

SURFACE DATA

	CURVATURE		THICKNESS		GLASS		
OBJ	0.00000000		1.00000E+11				
1	0.00000000		2.500000				
2	DECE	0.000000	0.000000	49.000000	0.000000	0.000000	
	0.00000000		.250000		ZNSE		
3	0.00000000		-.250000		REFL	ZNSE	
4	0.00000000		0.000000				
5	DECE	0.000000	0.000000	49.000000	0.000000	0.000000	
	0.00000000		-1.190000				
6	DECE	0.000000	-.100603	0.003000	0.000000	0.000000	RETU
	0.00000000		1.190000		REFL		
7	DECE	0.000000	0.000000	-49.000000	0.000000	0.000000	
	0.00000000		.500000		ZNSE		
8	0.00000000		0.000000				
9	DECE	0.000000	0.000000	49.003000	0.000000	0.000000	
	0.00000000		1.390000				
10	.35772000		.160000		ZNSE		
11	.12491253		2.766297		ZNS		
12	0.00000000		.040000				
13	0.00000000		.100000				
14	0.00000000		0.000000		GERM		
15	12.51324989		.040000				
16	15.84022167		.040000				
17	0.00000000		0.000000				
18	0.00000000		0.000000				